4

Laser Cladding Process Modeling

This chapter addresses the physics of the process along with several modeling techniques applied to the laser cladding by powder injection. Developed models assist us to improve and understand the underlying process and theory. These models can be used in the process prediction as well as designing a controller without performing any experiments. An accurate model is also important to reduce the cost of system development in an automated laser cladding process.

4.1 Physics of the Process

Figures 2.1 and 4.1 show the physical phenomena occurring in a laser cladding by powder injection process. The process can be sequentially listed as follows:

- The laser beam reaches the substrate and a significant part of its energy is directly absorbed by the substrate. A small part of laser energy is absorbed by powder particles. The energy absorbed by the substrate then develops a melt pool. The melted particles are simultaneously added into the melt pool (see Figure 2.1). This step of the process is expressed only by the heat conduction equation.

- Surface tension gradient drives the fluid flow within the melt pool. As far as the flow field penetrates in the substrate, the energy transfer mechanism changes to a mass convection mechanism. During this phenomenon, the melted powder particles are mixed rapidly in the melt pool (see Figure 4.1). This step of the process should be expressed by the momentum, the heat transfer, and continuity equations.

Based on these physical phenomena, three appropriate governing equations are heat conduction, continuity, and momentum.

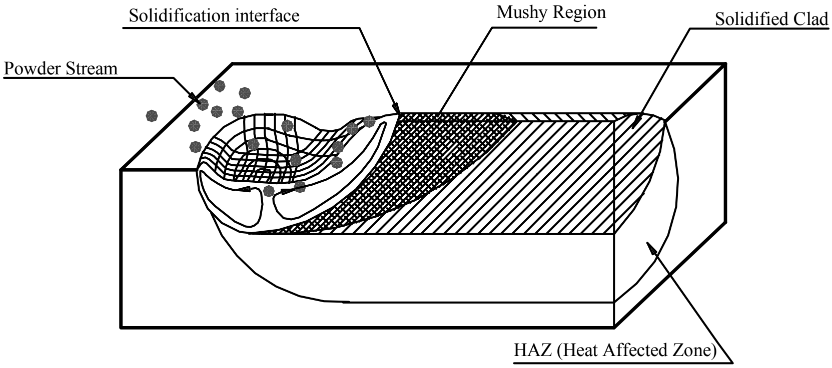

FIGURE 4.1
Schematic of convection influence during laser cladding process.

4.2 Governing Equations

For a laser cladding process, a moving laser beam with a general distribution intensity strikes on the substrate at $t = 0$ as shown in Figure 4.2. Due to additive material, the clad forms on the substrate as shown in the figure. The transient temperature distribution $T(x, y, z, t)$ is obtained from the three-dimensional heat conduction in the substrate as [156]:

$$\frac{\partial(\rho c_p T)}{\partial t} + \nabla \cdot (\rho c_p \mathbf{U} T) - \nabla \cdot (K \nabla T) = Q \tag{4.1}$$

where Q is power generation per unit volume of the substrate [W/m^3], K is thermal conductivity [W/m·K], c_p is specific heat capacity [J/kg·K], ρ is density [kg/m^3], t is time [s], and $\mathbf{U}$ is the travel velocity of the workpiece (process speed) [m/s].

In the laser cladding process, the conservation of momentum is one of the important governing laws. The equation of momentum is Newton's second law applied to fluid flow, which yields a vector equation. The momentum equation is represented as

$$\frac{\partial(\rho \mathbf{U})}{\partial t} + (\rho \mathbf{U} \nabla)\mathbf{U} = \rho \mathbf{g} - \nabla p + \mu \nabla \cdot (\nabla \mathbf{U}) \tag{4.2}$$

where $\mathbf{g}$ is gravity field [m/s^2], μ is viscosity [kg/s·m], and p is pressure [N/m^2].

The last equation is continuity and is represented by

$$\nabla \mathbf{U} = 0 \tag{4.3}$$

The above equations may be solved analytically (in special cases) or numerically along with required assumptions and/or simplifications.

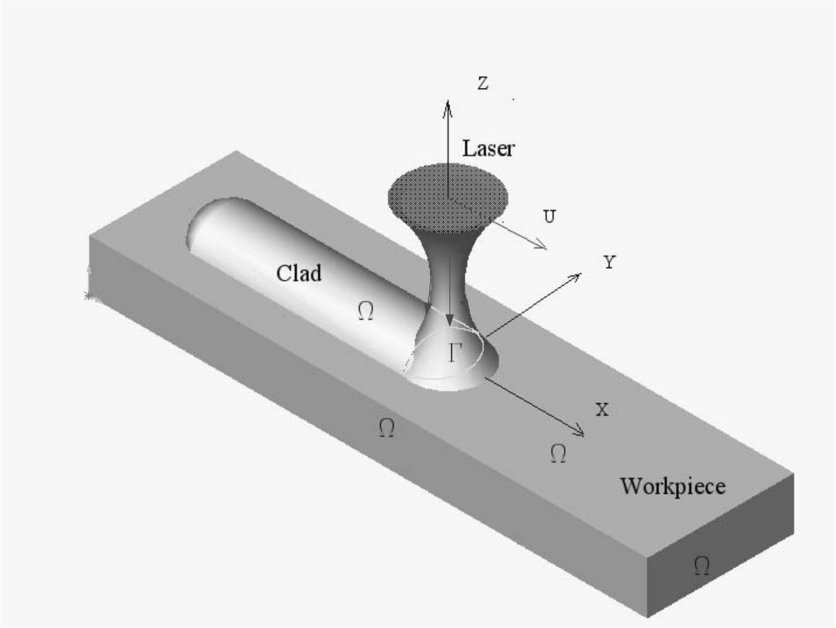

FIGURE 4.2
Schematic of the associated physical domains of the laser cladding process.

4.2.1 Essential Boundary Conditions

For the laser cladding process, a set of complicated boundary conditions should be satisfied. However, a set of important boundary conditions are as follows:

- The effect of the laser beam and the powder flux can be modeled as a surface heat source and heat flux, defined by the boundary condition as

$$-K(\nabla T \cdot \mathbf{n})|_{\Omega} = \begin{cases} \beta I(x,y,z,t) - h_c(T - T_0) - \epsilon_t \sigma (T^4 - T_0^4) & \text{if} \quad \Omega \in \Gamma \\ -h_c(T - T_0) - \epsilon_t \sigma (T^4 - T_0^4) & \text{if} \quad \Omega \notin \Gamma \end{cases} \tag{4.4}$$

  where $\mathbf{n}$ is the normal vector of the surface, $I(x,y,z,t)$ is the laser energy distribution on the workpiece [W/m^2], β is the absorption factor, h_c is the heat convection coefficient [W/m^2·K], ϵ_t is emissivity, σ is the Stefan-Boltzman constant [5.67×10^{-8} W/m^2·K^4], Ω is the workpiece surfaces [m^2], Γ is the surface area irradiated by the laser beam [m^2] and T_0 is the ambient temperature [K] [156].

- On the surface of the melt pool, if $\mathbf{g}$ is vertical, the surface tension should be derived by

$$\Delta p + \rho\, \mathbf{g}\, z = (2\mu \frac{\partial \mathbf{U}}{\partial n} \cdot \mathbf{n}) + \gamma / R \tag{4.5}$$

and

$$\mathbf{U} \cdot \mathbf{n} = 0 \tag{4.6}$$

where z is a vertical coordinate [m], γ is surface tension [N/m], and R is the clad surface curvature [m] [157].

- At the solid /liquid interface

$$f(x, y, z, t) = \text{Const.} \tag{4.7}$$

and

$$u_x = u_y = u_z = 0 \tag{4.8}$$

and

$$T = T_m \tag{4.9}$$

where $f(x, y, z, t)$ is a function that presents the melt pool interface with substrate, and u_x, u_y, and u_z is fluid velocity in x, y, and z directions, respectively [m/s] [158]. This condition is valid for pure elements. For the alloys, the freezing range should be considered.

- At initial time and infinite time, the following conditions should be satisfied

$$T(x, y, z, 0) = T_0 \tag{4.10}$$

and

$$T(x, y, z, \infty) = T_0 \tag{4.11}$$

4.3 Laser Cladding Models in Literature

Models, which are based on physical laws, contribute to better understanding of the laser cladding process. A precise model can support the required experimental research to develop laser cladding. Several steady-state models for laser cladding have been proposed, whereas few papers have dealt with the dynamic nature of the process. Steady-state models are those models that are independent of time, whereas dynamic models refer to those models that take into account the transient response of the process. Table 4.1 lists the papers that deal with modeling of laser cladding.

In the following, several developed models are briefly explained.

TABLE 4.1
List of modeling techniques and modeled paramaters for laser cladding.

Reference	Description
Chande et al., 1985, [159]	numerical model to obtain convection diffusion of matter in the melt pool
Kar et al., 1987, [160]	analytical model to obtain a diffusion model for extended solid solution
Hoadley et al., 1992, [157]	numerical model to obtain temperature field and longitudinal section of a clad track
Lemoine et al., 1993, [161]	analytical model to obtain powder efficiency
Picasso et al., 1994, [162]	numerical model to obtain clad geometry and melt pool temperature
Picasso et al., 1994, [163]	numerical model to obtain fluid motion, melt pool shape
Jouvard et al., 1997, [164]	analytical model to obtain critical energies for Nd: YAG cladding
Colaco et al., 1996, [165]	geometrical analysis to obtain clad height and powder efficiency
Romer et al., 1997, [166, 167]	analytical model to obtain temperature of the melt pool
Kaplan et. al , 1997, [168]	numerical model to obtain powder particles temperature, melting limits, melt pool cross section
Frenk et al., 1997, [136]	analytical model to obtain the total power absorbed by melt pool
Lin et al., 1998, [169]	numerical model to obtain powder catchment efficiency
Bambeger et al., 1998 [170]	analytical model to obtain the depth of clad and melt pool temperature
Romer et al., 1999, [171]	stochastic model to obtain melt pool temperature
Kim et al., 2000, [104]	numerical model to melt pool shape and dilution
Toyserkani et al., 2003, [172, 173]	numerical model to obtain clad bead geometry
Zhao et al., 2003 [174]	numerical model to obtain dilution, melt pool temperature
Toyserkani et al., 2002, [67, 134]	neural network and stochastic models to obtain the clad height
Labudovic et al., 2003, [175]	numerical model to obtain dimensions of fusion, residual stress and transient temperature profiles

4.3.1 Steady-State Models

Several analytical and numerical models have been developed to show the process dependencies on the process parameters. They address several important physical phenomena such as thermal conduction, thermocapillary (Marangoni) flow, powder and shield gas forces on melt pool, mass transport, diffusion, laser/powder interaction, melt pool/powder interaction, and laser/substrate interaction in the process zone.

Kar et al. [160] studied one-dimensional diffusion for extended solid solution in pre-placed laser cladding. They solved the energy transport and diffusion equations. They also obtained equations for the dimensions and composition of the clad layer restricted by many assumptions. These assumptions are: no convection in the melt pool, semi-infinite plane, cylindrical clad shape, thermal independent coefficients, and two-stage laser cladding. They improved their model by considering the heat convection in the surface and finding a model for changing the partition coefficient [176].

Hoadley et al. [157] developed a two-dimensional finite element model for powder injection laser cladding. The model simulated the quasi-steady temperature field for the longitudinal section of a clad track. They took into account the melting of the powder particles in the liquid pool and liquid/gas free surface shape and position. Their results are for an idealized problem, where there is almost no melting of the substrate material in the clad. The results also demonstrate the linear relationship between laser power, the processing velocity, and the thickness of the deposited layer.

One of the most simple but realistic models was obtained by Picasso et al. [162]. They considered the interaction between the powder particles and laser beam in the melt pool. They assumed the particles were melted by the laser beam before they arrived in the melt pool. The model predicted some of the processing parameters of laser cladding, including the beam velocity, the powder feed rate in the given laser power, beam width, and geometry of the powder injection jet. Picasso et al. [163] also developed a two-dimensional, stationary, finite element model for laser cladding by considering heat transfer, fluid motion, and deformation of the liquid-gas interface. They solved a stationary Stephan equation and found the shape of the melt pool in a known clad height

Lin et al. [145], [177], and [169] developed a simple model for laser cladding with a coaxial nozzle. This model was proposed to characterize the particle bonding under heating in the cladding process. The results showed that particle sticking on the clad surface was increased when the particle size, velocity and the bonding temperature were decreased.

Frenk et al. [136] developed a quantitative analytical model of the process based on the overall mass and energy balance. This model allowed them to calculate the mass efficiency and the global absorptivity for laser cladding of Stellite 6 powder on mild steel, taking into account the incorporation of the powder into the melt pool as well as the energy absorbed by the powder jet and the substrate.

Colaco et al. [165] developed a simple lumped model for correlation between the geometry of laser cladding tracks and the process parameters. They assumed a circular shape for the cross sections of the laser clad tracks. Based on their results, a correlation between width and height of clads with the operating parameters such as powder feed rate, the process speed and efficiency of the powder was obtained.

Lemoine et al. [161] developed a model to predict laser cladding parameters such as the laser power and powder feed rate for a desired temperature. They considered a homogeneous temperature distribution inside each powder particle during the interaction time.

Romer et al. [166] obtained an analytical process model, which relates the depth of the melt pool to the laser power and relative velocity of the laser beam to the sample. This model accounted for the latent heat of fusion and energy produced in the melt pool by exothermic reactions within the melt pool. The model showed a linear dependence of the melt pool depth on laser power and an inverse dependence on the square root of the relative beam velocity.

Jouvard et al. [164] developed a model for an Nd:YAG laser operated at low powers, typically less than 800 W. Their theoretical study relied on a calculation of the powder feed rate fed into the melt pool and on a model of heat transfer in the substrate. They realized that the first power threshold is the power required for substrate melting, the second power threshold is the power that melts the powder particles directly and therefore they are in liquid phase when contacting the substrate.

4.3.2 Dynamic Models

An important step in control of laser cladding is to find a precise dynamic model for it. Bamberger et al. [170] developed a simplified theoretical model for estimating the operating parameters of laser surface alloying and cladding by the direct injection of powder into the melt pool. They developed an analytical dynamic expression for laser cladding when the table velocity was related to the melt pool temperature. They also achieved a steady-state expression, which related the height of the clad to the velocity of the table.

The work done by Kim et al. [104] has modeled the melt pool formed during laser cladding by wire feeding using a two-dimensional, transient finite element technique.

Due to the complexity of laser material processing, several authors have tried to identify a dynamic model for different methods of laser material processing using system identification techniques; however, there seems to be no report regarding the laser cladding dynamic model prediction using such techniques.

Battaille et al. [178] tried to identify a dynamic model for laser hardening by system identification methods. They used a preliminary identification experiment with a pseudo random binary sequence (PRBS).

Romer et al. [171] found a stocastic-based dynamic model for the laser alloying process, when the table velocity or laser power was selected as the input and the melt pool surface area as the output. They used the auto regressive exogenous (ARX) system identification technique to obtain a dynamic model for laser alloying. The authors recognized nonlinearity in the process and, as a result, they used a linearized model for an operating point. They have reported that their model has performed poorly in many different cases due to its operating point dependency.

4.4 Lumped Models

In a lumped model, the dependency of the process (equations) and spatial variables is ignored and time becomes the only independent variable. This simplification will render ordinary differential equations as opposed to partial differential equations. In laser cladding by powder injection, a lumped model can be proposed by a balance of energy in the process.

The balance of energy in the process is shown in Figure 4.3. In the figure, the total laser energy absorbed by the substrate and powder particles as well as different source of losses (e.g., reflection, radiation and convection) are shown. The balance of energy can be expressed by

$$Q_c = Q_l - Q_{rs} - Q_L + (\eta - 1)Q_p - Q_{rp} - Q_{radiation} - Q_{convection} \quad (4.12)$$

where Q_c is the total energy absorbed by the substrate [J], Q_l is laser energy [J], Q_{rs} is reflected energy from substrate, Q_L is latent energy of fusion [J], η is powder catchment efficiency, Q_p is energy absorbed by powder particles [J], Q_{rp} is reflected energy from powder particles [J], $Q_{radiation}$ is energy loss due to radiation [J], and $Q_{convection}$ is energy loss due to convection [J].

The laser energy is presented by

$$Q_l = A_l P_l t_i = \pi r_l^2 P_l t_i \quad (4.13)$$

where A_l is the laser beam area on the substrate [m^2], r_l is the beam spot radius on the substrate [m], P_l is laser average power [W], and t is interaction time between the material and laser [s] which is presented by

$$t_i = \frac{2r_l}{U} \quad (4.14)$$

The process speed is shown by U [m/s].

The reflected energy from the substrate is

$$Q_{rs} = (1 - \beta_w)(Q_l - Q_p) \quad (4.15)$$

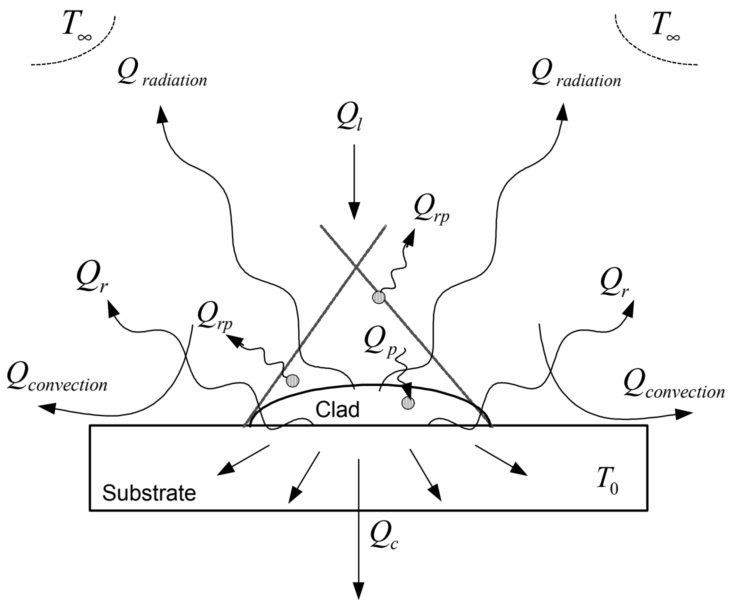

FIGURE 4.3
Balance of energy in laser cladding by powder injection.

where β_w is workpiece absorbed coefficient.

The latent heat energy can be expressed by

$$Q_L = L_f \rho V \tag{4.16}$$

where L_f is latent heat of fusion [J/kg], ρ is average density in clad area [kg/m^3] and V is the volume of melt pool, including the clad region [m^3].

In order to find an expression for V in a lumped fashion, we can consider a portion of a cylinder laying on the substrate as shown in Figure 4.4, where the width of the clad is equal to the laser beam diameter on the substrate. Also, we assume that the length of the melt pool is equal to the laser beam diameter. The cross section area A_c can be found by

$$A_c = \frac{\dot{m}}{\rho_p U}\eta \tag{4.17}$$

where ρ_p is particles density [kg/m^3]. If dilution is ignorable, which is an appropriate assumption for laser cladding, and the width of the melt pool is equal to laser diameter, the volume of melted area V can be expressed by

$$V = 2r_l A_c \tag{4.18}$$

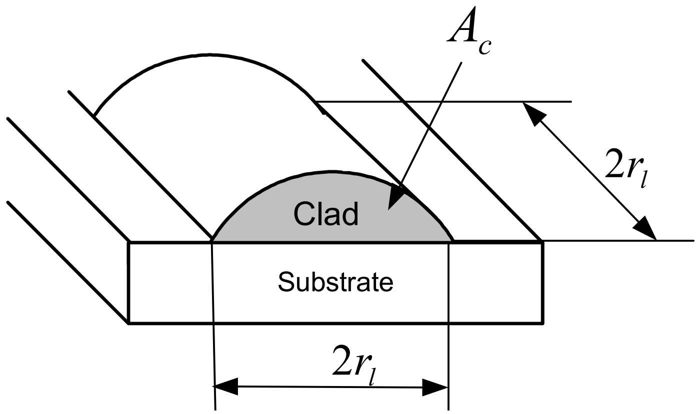

FIGURE 4.4
A lumped cross section of the clad and substrate.

In a lumped model, the powder efficiency can be assumed as the ratio between the area of laser beam and powder stream on the substrate. Therefore

$$\eta = \frac{r_l^2}{r_s^2} \tag{4.19}$$

where r_s is the powder stream diameter on the substrate [m].

In order to derive an equation for the energy absorbed by powder particles in a lumped model, consider a homogeneous distribution of powder particles over the laser beam cross section as shown in Figure 4.5. If powder particle radius r_p is known, the number of particles n in the laser beam area over a time period of t_i is given by

$$n = \frac{3\dot{m}t_i}{4\pi\rho_p r_p^3} \tag{4.20}$$

where $\dot{m}$ is powder feed rate [kg/s], and ρ_p is powder density [kg/m^3].

The overall area of the powder particles in the laser beam indicates the attenuated area A_{at} [m^2] by the powder particles as

$$A_{at} = n\pi r_p^2 = \frac{3\dot{m}t_i}{4\rho_p r_p} \tag{4.21}$$

As a result, the absorbed energy by the particles can be obtained by

$$Q_p = Q_l \frac{A_{at}}{A_l} = \frac{3Q_l\dot{m}t_i}{4\pi\rho_p r_p r_l^2} \tag{4.22}$$

The reflected energy from the powder particles can be derived from

$$Q_{rp} = (1-\beta_p)Q_p \tag{4.23}$$

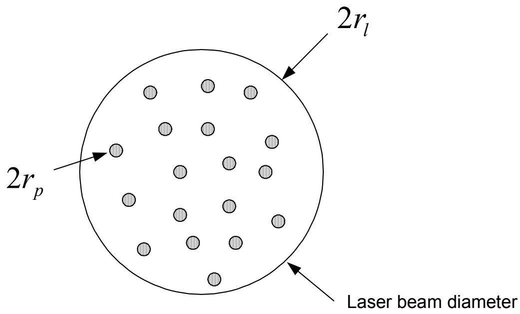

FIGURE 4.5
Attenuated area by powder particles.

where β_p is powder particles' absorbed coefficient.

The radiative loss can be presented by

$$Q_{radiation} = A_l \epsilon_t \sigma (T^4 - T_0^4) \tag{4.24}$$

where ϵ_t is emissivity, σ is the Stefan-Boltzman constant [5.67×10^{-8} W/m^2·K^4], T is melt pool temperature [K], and T_0 is ambient temperature [K].

The convective loss in a lumped model, assuming a concentrated heating zone in the laser beam area, can be presented by

$$Q_{convection} = A_l h_c (T - T_0) \tag{4.25}$$

where h_c is the heat convection coefficient [W/m^2·K]. Calculating h_c is difficult and Goldak [179] and Yang [180] suggested an experimental expression, which is

$$h_c = 24.1 \times 10^{-4} \epsilon_t T^{1.61} \tag{4.26}$$

Equation (4.26) introduces a nonlinear term in the final energy balance equation. This term can, however, be ignored for simplification of final differential equation.

The energy Q_c can be presented in an integral form as

$$Q_c = \rho c_p \int_{V_s} T(x, y, z, t_i) dV_s \tag{4.27}$$

where V_s is the heat-affected volume in Cartesian coordinates (x, y, z) [m^3] and ρ is the average density in the clad region [kg/m^3].

Substitution of the parameters in Equation (4.12) leads to an equation for Q_c. Plugging the derived equation for Q_c into Equation (4.27) leads to a lumped differential equation that presents the lumped model of the process. This differential equation can be solved by different numerical approaches.

4.5 Analytical Modeling

In general, there is no closed form solution for an analytical model with both heat conduction and momentum equations for the laser cladding process. However, when only heat conduction is considered for a moving heat source, the solution can be found. A well-known approach to solve the simplified heat conduction Equation (4.1) with given boundary and initial conditions is Green's function [156]. Based on this function the temperature distribution at time t and point (x, y, z) is represented as

$$T(x,y,z,t) = T_0 + \int_0^t \int_{-\infty}^{+\infty} \int_{-\infty}^{+\infty} G(x,y,z,t,x',y',0,t',u)\beta I(x',y',t')dx'dy'dz' \quad (4.28)$$

where

$$G(x,y,z,t,x',y',0,t',u) = \frac{1}{4\sqrt{k}[\pi(t-t')]^{3/2}K} \exp\left\{\frac{[(x-x')+u(t-t')]^2+(y-y')^2+z^2}{-4k(t-t')}\right\} \quad (4.29)$$

and

$$k = \frac{K}{\rho c_p} \quad (4.30)$$

$T(x, y, z, t)$ [K] represent the temperature at (x, y, z) at time t [s] due to a point source of laser generated at (x', y', z') at time t' [s] that is moving with velocity of u [m/s], K is thermal conductivity [W/m·K], c_p is specific heat capacity [J/kg·K], ρ is density [kg/m^3], and T_0 is ambient temperature [K].

In order to evaluate the steady-state and transient part, Green's function can be rewritten as the product of a steady-state term W and a time-dependent term V as

$$G(x,y,z,t,x',y',0,t',u) = W(x,y,z,x',y,u)V(x,y,z,t,x',y',t',u)$$

where

$$W(x,y,z,x',y',u) = \frac{1}{2\pi K\chi}\exp[-\frac{u}{2k}(x-x'+\chi)] \quad (4.31)$$

and

$$V(x,y,z,t,x',y',t',u) = \frac{\chi}{2\sqrt{\pi k}(t-t')^{3/2}}\exp\left\{-\frac{[\chi-u(t-t')]^2}{4k(t-t')}\right\} \quad (4.32)$$

where

$$\chi = \sqrt{(x-x')^2+(y-y')^2+z^2} \quad (4.33)$$

After reversing the order of integration, the temperature distribution Equation (4.1) can be written as

$$T(x,y,z,t) = T_0 + \int_{-\infty}^{+\infty}\int_{-\infty}^{+\infty} \beta I(x', y', t') W(x,y,z,x',y,u) V'(\chi, t, u) dx' dy' \quad (4.34)$$

where

$$V'(\chi, t, v) = \int_0^t U(x,y,z,t,x',y',t',u) dt' \quad (4.35)$$

which can be rewritten, using $\xi = \frac{1}{\sqrt{k(t-t')}}$ as

$$V'(\chi,t,v) = \frac{\chi}{\sqrt{\pi}} \int_{1/\sqrt{kt}}^{\infty} \exp[-\frac{(\chi\xi^2 - u/k)^2}{4\xi^2}] d\xi \quad (4.36)$$
$$= \frac{1}{2}\left\{1 - \operatorname{erf}(\frac{\chi - ut}{2\sqrt{kt}}) + \exp[\chi v/k)(1 - \operatorname{erf}(\frac{\chi + ut}{2\sqrt{kt}})]\right\}$$

As an example, when the substrate is Fe, the laser beam is at $(0, 0)$ position, and process speed is 0.005 m/s; W and V' for different χ are shown in Figures 4.6a and 4.6b, respectively. The W plot represents the steady-state nature of the thermal domain, whereas the V plot shows the time dependency of the thermal domain.

In the following section, we present a case study based on numerical solution of the laser cladding process.

4.6 Numerical Modeling – A Case Study

As a case study, we develop a numerical model for the laser cladding by powder injection. The main objective of developing a 3-D transient finite element model of laser cladding by powder injection is to investigate the effects of laser pulse shaping, traveling speed and powder feed rate on the clad geometry as a function of time.

To improve and understand the underlying process and theory, several models have been developed in the literature as addressed before. These models show the dependence of the process on the important parameters involved. These models can also be used in predicting the process for different parameters as well as controller design. An accurate model can significantly reduce the development cost of automated laser cladding systems.

Although the literature indicates several laser cladding models, there is a significant lack of more accurate models that take into account the effects of

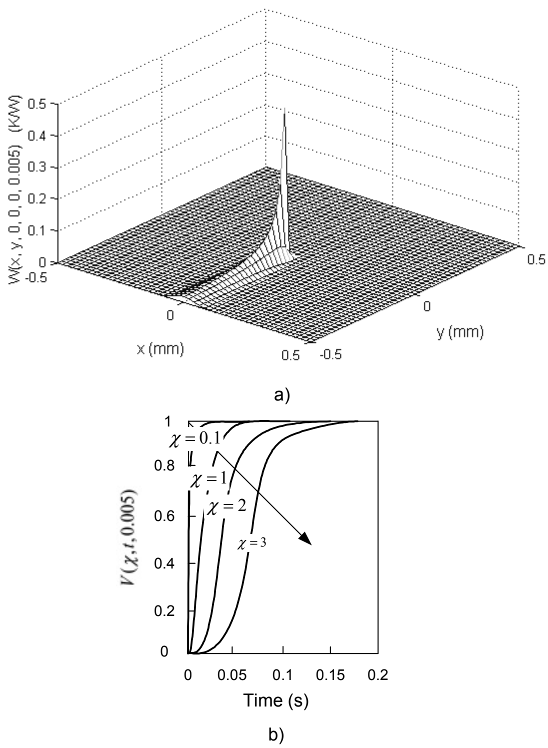

FIGURE 4.6
a) Illustration of a typical value for function W, in which the laser beam is in the center of the plane $(0, 0)$, the velocity of laser beam is 0.005 m/s, and the material is Fe under a CO_2 beam, b) illustration for V' vs. time for different χ.

laser pulse characteristics, melt pool geometry, power attenuation due to the powder particles, absorption factor deviation during the process (Brewster effect), and temperature dependencies of material properties. The literature also shows the absence of a model for the prediction of the clad geometry in the transient and dynamic period of the process.

In order to develop a more precise model, a solution strategy is proposed. In this strategy, the interaction between the powder and the melt pool is assumed to be decoupled and as a result, the melt pool boundary is first obtained in the absence of powder spray. Once the melt pool boundary is calculated, it is assumed that a layer of coating material based on powder feed rate and elapsed time is deposited on the intersection of the melt pool and powder stream in the absence of laser beam. The new melt pool boundary is then calculated by thermal analysis of the deposited powder layer, substrate, and laser heat flux.

For implementation of the proposed solution strategy, a finite element technique is used to develop a novel 3-D transient model for laser cladding by powder injection. The model is then used to study the correlation between the clad geometry and the process parameters. In the first set of simulations, the effects of laser pulse shaping parameters (laser pulse frequency and energy) on the clad geometry are investigated when the other process parameters such as travel speed, laser pulse width, powder jet geometry and powder feed rate are constant. In the second set of simulations, the effects of the process speed and powder feed rate on the clad geometry are investigated when laser pulse shaping including energy, frequency and width of the pulse and powder jet geometry are constant.

The quality of cladding of Fe on mild steel for different parameter sets is experimentally evaluated and shown as a function of effective powder deposition density and effective energy density. The comparisons between the numerical and experimental results are also presented.

In the following section, a thermal mathematical model is developed and required assumptions are addressed.

4.6.1 Thermal Mathematical Model

For a laser cladding process, a moving laser beam with a Gaussian distribution intensity strikes the substrate at $t = 0$ as is shown in Figure 4.2. Due to material added, the clads form on the substrate as shown in the figure. The transient temperature distribution $T(x, y, z, t)$ is obtained from the three-dimensional heat conduction in the substrate as expressed by Equation (4.1) [156]. As discussed earlier, the boundary conditions for the heat transfer process are Equations (4.4), (4.10) and (4.11).

Equation (4.1) along with boundary conditions (4.4), (4.10) and (4.11) cannot comprehensively express the physics of the process. Therefore, to incorporate the effects of the laser beam shaping, latent heat of fusion, Marangoni phenomena, geometry growing(changing the geometry), and Brewster effect, the following adjustments are considered:

- A pulsed Gaussian laser beam with a circular mode (TEM_{00}) [101] is considered for the beam distribution. The laser power distribution profile I [W/m^2] is [181]

$$I(r) = \delta\, I_0 \exp\left[-\left(\frac{\sqrt{2}}{r_l}\right)^2 r^2\right] \tag{4.37}$$

where

$$r = \sqrt{x^2 + y^2}\,, \qquad I_0 = \frac{2}{\pi r_l^2} P_l\,, \quad \text{and} \qquad P_l = EF \tag{4.38}$$

and r_l is the beam radius [m], I_0 is intensity scale factor [W/m^2], P_l is the laser average power [W], E is the energy per pulse [J], and F is the laser pulse frequency [Hz]. When the laser beam is on $\delta = 1$ and when it is off $\delta = 0$. The parameter δ is changed based on the laser pulse shaping parameters such as frequency F and width W that is the time that the laser beam is on in one period.

- The effect of latent heat of fusion on the temperature distribution can be approximated by increasing the specific heat capacity [182], as

$$c_p^* = \frac{L_f}{T_m - T_0} + c_p \tag{4.39}$$

where c_p^* is modified heat capacity [J/kg·K], c_p is the original heat capacity [J/kg·K], L_f is latent heat of fusion [J/kg], T_m is melting temperature [K], and T_0 is ambient temperature [K].

- The effect of fluid motion due to the thermocapillary phenomena can be taken into account using a modified thermal conductivity for calculating the melt pool boundaries. Experimental work and estimations in the literature [183] suggest that the effective thermal conductivity in the presence of thermocapillary flow is at least twice the stationary melt conductivity. This increase can be generally presented by

$$K^*(T) = aK(T_m) \qquad \text{if} \quad T > T_m \tag{4.40}$$

where a is the correction factor and K^* is modified thermal conductivity [W/m·K].

- Power attenuation is considered using the method developed by Picasso et al. [162] with some minor modifications. Figure 4.7 shows the proposed geometrical characteristics in the process zone which is used in the development of the following equations. Based on their work

$$P_1 = P_l \beta_w(\theta) \left(1 - \frac{P_{at}}{P_l}\right) \tag{4.41}$$

$$P_2 = P_l \eta_p \beta_p \frac{P_{at}}{P_l} \left[1 + (1 - \beta_w(\theta)) \left(1 - \frac{P_{at}}{P_l}\right)\right] \tag{4.42}$$

where P_1 is total power directly absorbed by the substrate [W], P_2 is power that is carried into the melt pool by powder particles [W], P_{at} is attenuated laser power by the powder particles [W], $\beta_w(\theta)$ is workpiece absorption factor, β_p is particle absorption factor, and θ is the angle of the top surface of the melt pool with respect to the horizontal line as shown in Figure 4.7 [deg]. Consequently, the total power absorbed by the workpiece P_w [W] is

$$P_w = P_1 + P_2 = \beta P_l \tag{4.43}$$

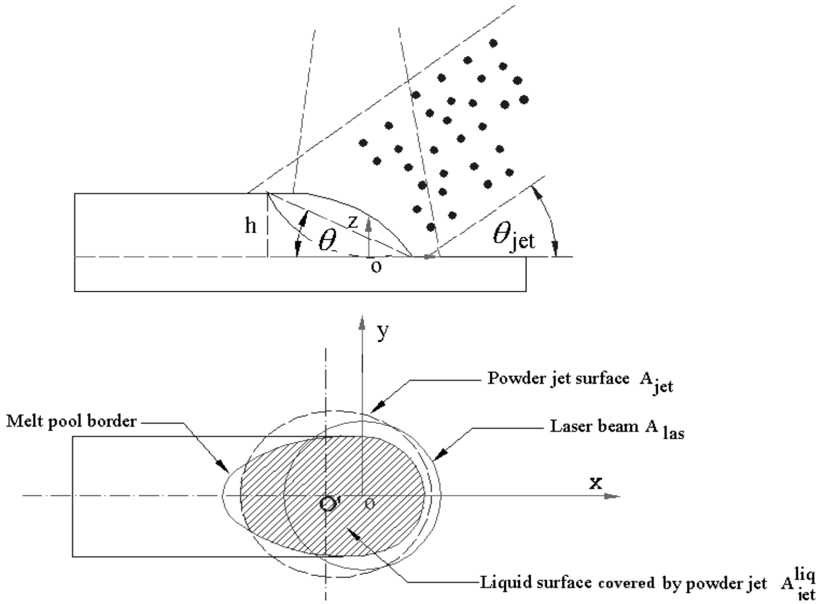

FIGURE 4.7
The proposed geometrical characteristics of process zone.

where β is the modified absorption factor.

The ratio between the attenuated and average laser power can be obtained by [162]

$$\frac{P_{at}}{P_l} = \begin{cases} \frac{\dot{m}}{2\rho_c r_l r_p v_p \cos(\theta_{jet})} & \text{if} \quad r_{jet} < r_l \\ \frac{\dot{m}}{2\rho_c r_{jet} r_p v_p \cos(\theta_{jet})} & \text{if} \quad r_{jet} \geq r_l \end{cases} \tag{4.44}$$

In these equations, $\dot{m}$ is powder feed rate [kg/s], ρ_c is powder density [kg/m^3], r_l is radius of the laser beam on the substrate [m], r_p is radius of powder particles [m], v_p is powder particles velocity [m/s], θ_{jet} is the angle between powder jet and substrate [deg], and r_{jet} is radius of powder spray jet [m]. The powder catchment efficiency η_p can be considered as the ratio between the melt pool surface and the area of powder stream (Figure 4.7) as

$$\eta_p = \frac{A_{jet}^{liq}}{A_{jet}} \tag{4.45}$$

where A_{jet}^{liq} is the intersection between the melt pool area on the workpiece and powder stream, and A_{jet} is the cross-section area of the powder stream on the workpiece.

If we assume the absorption of a flat plane inclined to a circular laser beam depends linearly on the angle of inclination θ as shown in Figure 4.7, and $\beta_w(0)$ is the workpiece absorption of a flat surface, $\beta_w(\theta)$ can be calculated from

$$\beta_w(\theta) = \beta_w(0)(1 + \alpha_w \theta) \tag{4.46}$$

where θ is the angle shown in Figure 4.7 and α_w is a constant coefficient obtained experimentally for each material [101], [162].

- The temperature dependency of material properties and absorption coefficients on the temperature are taken into account in the model.

- In order to reduce the computational time, a combined heat transfer coefficient for the radiative and convective boundary conditions is calculated based on the relationship given by Goldak [179] and Yang [180]:

$$h_c = 24.1 \times 10^{-4} \epsilon_t T^{1.61} \tag{4.47}$$

Using (4.47), (4.37), and (4.43), the boundary condition in (2.2) is simplified to

$$-K(\nabla T \cdot \mathbf{n})|_\Omega = \begin{cases} \frac{2}{\pi r_l^2} \delta \beta P_l \exp\left[-\left(\frac{\sqrt{2}}{r_l}\right)^2 r^2\right] - h_c(T - T_0) & \text{if} \quad \Omega \in \Gamma \\ -h_c(T - T_0) & \text{if} \quad \Omega \notin \Gamma \end{cases} \tag{4.48}$$

4.6.2 Solution Algorithm

A method can be proposed to obtain the clad geometry in a 3-D and time-dependent laser cladding process using the model discussed in the previous section. This proposed numerical solution has two steps as follows:

1. Obtaining the melt pool boundary in the absence of the powder spray. In this step, the interaction between the powder and melt pool is assumed to be decoupled, and, as a result, the melt pool boundary can be obtained by solving Equation (4.1).

2. Adding a layer of the powder to the workpiece in the absence of the laser beam. In this step, once the melt pool boundary is calculated, it is assumed that a layer of coating material based on the powder feed rate, elapsed time, and intersection of melt pool/powder jet is deposited on the workpiece. The new deposited layer creates a new tiny object on the previous domain which is limited to the intersection of the powder stream and the melt pool. For each increment in time, Δt, its height is given by

$$\Delta h = \frac{\dot{m} \Delta t}{\pi r_{jet}^2 \rho_c} \tag{4.49}$$

where Δh is the thickness of the deposited layer [m] and Δt is the elapsed time [s]. For numerical convergence, the temperature profile of the added layer is assumed to be the same as the temperature of the underneath layer, which will be discussed in the end of this section. The new temperature profile of the combined workpiece and the layer of powder is then obtained by repeating Step 1.

Figure 4.8 shows the sequence of the proposed numerical modeling. On the left side of the figure, a moving laser beam is shown while the deposition of coating material (Step 2) is presented on the right side. The numerical solution is carried out in two different time periods. The first one is the time between two deposition steps, and the second one is the time period for calculating the melt pool area.

After performing Step 2 and before repeating the first step, the following corrections are applied:

- All thermo-physical properties and absorption factor $\beta_w(0)$ are updated based on the new temperature distribution.
- The new $\beta_w(\theta)$ is calculated based on the updated θ and Equation (4.46).
- The new η_p is obtained based on the new melt pool geometry using Equation (4.45).
- The new P_w is calculated using Equation (4.43).

Many numerical methods for solving Equation (4.1) have been reported since 1940. Finite element method (FEM) is one of the most reliable and efficient numerical techniques, which has been used for many years. FEM can solve different forms of partial differential equations with different boundary conditions. In this work, the governing PDE Equation (4.1) is highly nonlinear due to material properties with dependency on temperature and a moving heat source with a Gaussian distribution.

To implement the numerical solution strategy, code was developed using the MATLAB (www.mathworks.com)/ FEMLAB (www.femlab.com) software. The code discretizes the heat conduction equation and generates the initial mesh in the substrate using the available options in FEMLAB. By solving Equation (4.1) and calculating the melt pool boundary, the geometry of the domain is modified to incorporate the clad into the substrate. For meshing, the domain is partitioned into tetrahedrons (mesh elements) as shown in Figure 4.10. Due to the deposited layer and changes in the substrate geometry, an adaptive meshing strategy is used. As it is seen, the mesh is finer for the portion of the domain in which the clad is generated. A time-dependent solver is used to solve the nonlinear time-dependent heat transfer equation. The solver is an implicit differential-algebraic equation (DAE) solver with

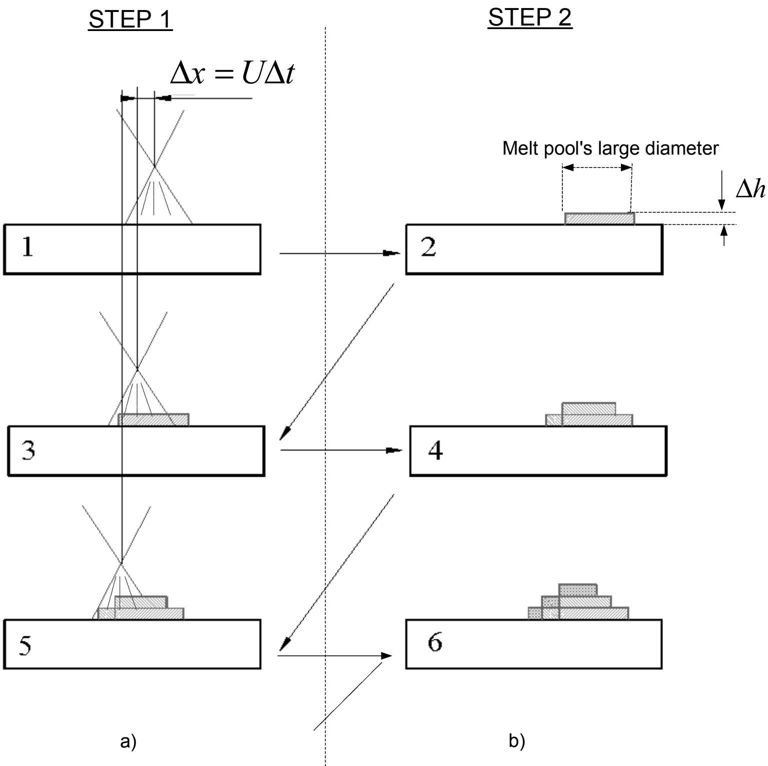

FIGURE 4.8
Sequence of calculation in the proposed numerical model: a) Step 1, b) Step 2.

automatic step size control which is patented as *fldask* [184]. The solver is suitable for solving equations with singular and nonlinear terms.

To justify the assumption made in Step 2 of the solution strategy regarding the temperature of the added layer, we note that the power transferred to the workpiece by the powder particles is considered by Equation (4.42). As a result, the temperature of the deposited layer in Step 2 should be assumed to be the same as the ambient temperature, which we consider contrary to it to be the same as that of the melt pool of the underneath layer. Numerical calculation indicates that this added energy is about 1% of the power, which does not have a considerable effect on the overall results. This assumption will help the convergence of the numerical solution and reduction of the computational time by eliminating the large temperature gradient between the added and underneath layers which cause instability in most of today's numerical solvers.

TABLE 4.2
Process parameters.

r_l [m]	$7.0e-4$ [187]	T_0 [K]	293 [185]
r_p [m]	$22.5e-6$	T_v [K]	3313 [185]
r_{jet} [m]	$7.5e-4$	T_m [K]	1811 [185]
Laser pulse width [ms]	3	v_p [m/s]	26
α	$1.67e-2$ [162]	θ_{jet} [deg.]	55
a	2.5 [183]	β_p [%]for Nd:YAG	34 [186]

In the following section, the numerical parameters that are considered for the numerical model are addressed.

4.6.3 Numerical Parameters

A $50 \times 10 \times 5$ mm block is selected for the initial substrate in a Cartesian coordinate system as shown in Figure 4.10. The thermo-physical properties of Fe are considered for both substrate and powder. All thermo-physical properties such as thermal conductivity, specific thermal heat, emissivity and density are considered to be temperature dependent. The thermo-physical properties for temperatures higher than vapor temperature, T_v, are fixed to the amount of thermo-physical properties in T_v. All the thermo-physical parameters have been obtained from Wong [185]. Also, $\beta_w(0)$ as a function of temperature is obtained from Xie and Kar [186] for Fe when a Nd:YAG laser is used. The other process parameters are listed in Table 4.2.

In order to investigate the independence of the solutions on the number of nodes, simulations were performed in the different number of nodes. The computational results are shown in Figure 4.9. As seen, with increase of number of nodes, the curve shows the calculated temperatures at $x = 0.030$ m, $y = 0.000$ m, $z = 0.005$ m and at $t = 20$ s becomes flat such that the difference between the calculated temperatures with $8,100$ and $10,203$ nodes is 8 K. As a result, the number of elements was initialized with $10,203$ nodes and $43,577$ elements which were mostly concentrated on the top of the surface as seen in Figure 4.10. The simulation was performed for 20 seconds. The time step between layers' depositions was set to 20 ms and the other time step was controlled by the solver; however, it was not greater than 0.2 ms.

The developed software was then used in studying the laser cladding process for different physical parameters.

4.6.4 Numerical Results

Simulations were carried out for different process parameters to study various aspects of laser cladding, which can be categorized into two sections as follows:

1. In the first study, the effects of laser pulse shaping on the clad geometry

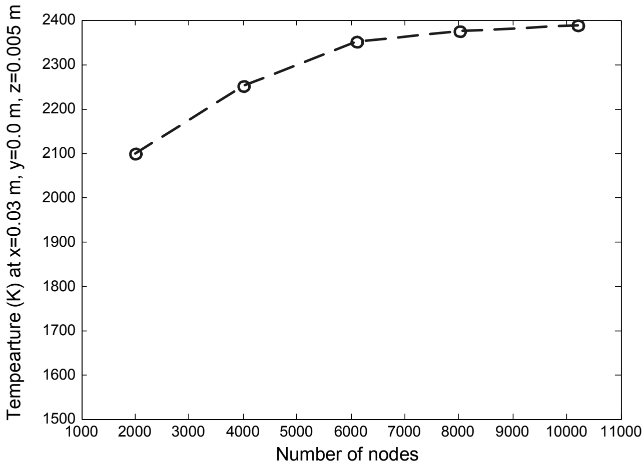

FIGURE 4.9
Comparison between the calculated temperature at a desired point in different number of nodes to investigate the independency of solutions on the number of grid.

were investigated when the other process parameters were constant.

2. In the second study, the effects of travel speed and powder feed rates on the clad geometry were examined when the other parameters were constant.

In the following section, these two studies along with a selection of 3D numerical results will be addressed.

4.6.4.1 Effects of Laser Pulse Shaping on Clad Geometry

In order to evaluate the contribution of the laser pulse energy E and the laser pulse frequency F on the clad geometry, a multistep laser pulse energy and pulse frequency were selected as shown in Figures 4.11a and 4.11b, respectively. The laser pulse energy was changed from 2.5 J to 4 J in four steps. The laser pulse frequency was also changed from 70 to 100 Hz in four steps. The average laser power for both cases are shown in Figures 4.11a and 4.11b. In the numerical simulations of the first study, $U = 0.001$ m/s and $\dot{m} = 1.67e - 5$ kg/s. Also, in all numerical simulations, it was assumed that the laser was turned on at $t = 0$ s and the beam was at a position of $x = 10$, $y = 0$ and $z = 5$ mm.

Figure 4.12 shows the temperature distribution of the workpiece at $t = 20$ s in different views for a multistep laser pulse energy. The figure illustrates the isothermal lines in the domain where the maximum temperature was $2,388$

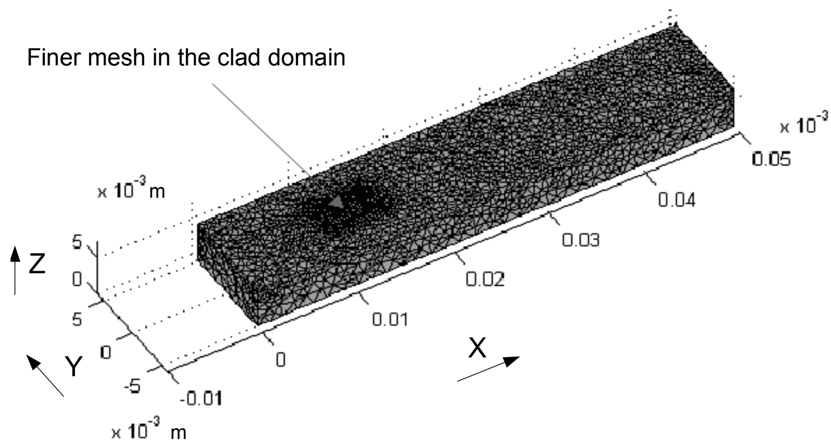

FIGURE 4.10
A typical mesh in the proposed domain.

K. It also shows a rapid cooling in the domain due to the concentrated moving heat source. Along the object, the isothermal lines expand, whereas the condensed isothermal lines exist in the area close to the laser source.

Figure 4.13 shows the generated clad after 20 s for a multistep laser pulse energy. In order to have a better view of the generated clad on the substrate, a virtual light source to illuminate the domain is considered. The ripples on the generated clad were discovered to be dependent on the size, shape and number of elements used to mesh the domain. Increasing the number of meshes can reduce the ripples; however, the average height remains the same. Although increases in the number of meshes and reducing their size result in elimination of ripples, the computational time dramatically increases.

As seen in Figures 4.12 and 4.13, the clad height and width increase with increasing laser pulse energy as expected.

4.6.4.2 Effects of Process Speed and Powder Feed Rate on Clad Geometry

In order to evaluate the contribution of the travel speed, U, and the powder feed rate, $\dot{m}$, on the clad geometry, a multistep travel speed is applied to the numerical procedure for five different powder feed rates. The selected multistep speed is shown in Figure 4.14. This multistep speed is applied for five different feed rates: $\dot{m}_1 = 1.67e-5$, $\dot{m}_2 = 2.09e-5$, $\dot{m}_3 = 2.51e-5, \dot{m}_4 = 2.92e-5$, and $\dot{m}_5 = 3.34e-5$ kg/s. For all numerical simulations, laser pulse energy is $E = 3.5$ J, laser pulse frequency $F = 100$ Hz and laser pulse width is $W = 3$ ms..

Figure 4.15 shows the temperature distribution of the workpiece at

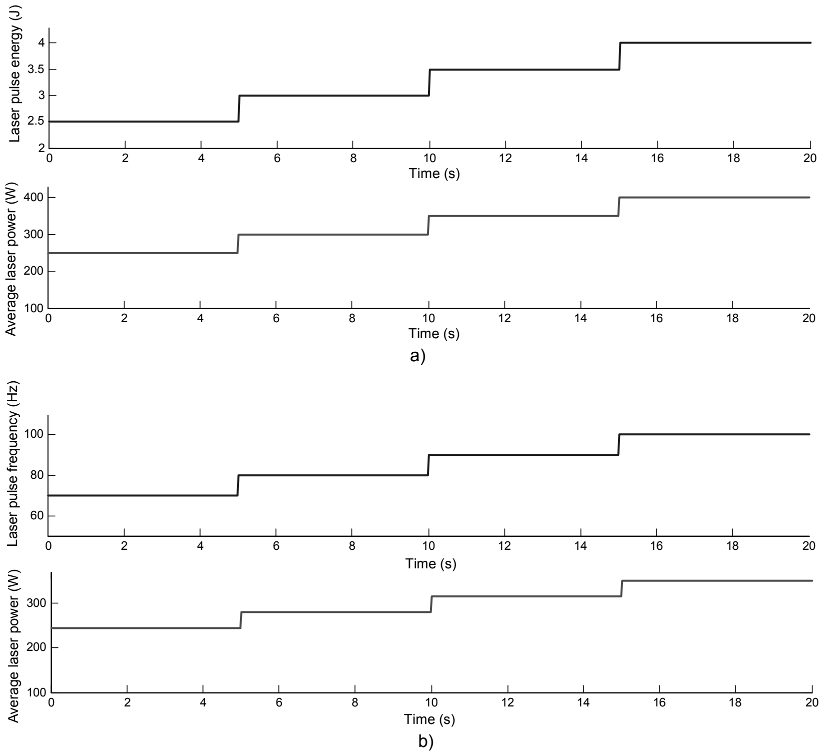

FIGURE 4.11
a) Multistep laser pulse energy along with corresponding average laser power, b) Multistep laser pulse frequency along with corresponding average laser power.

$t = 20$ s for a multistep velocity at $\dot{m}_1 = 1.67e - 5$ kg/s in different views. The figure illustrates the isothermal lines in the whole domain where the maximum temperature is $2,030$ K. The figure also shows a rapid cooling in the domain due to the concentrated moving heat source. Along the object, the isothermal lines expand whereas the condensed isothermal lines exist in the area close to the laser source.

Figure 4.16 shows the effect of powder feed rate on the maximum temperature in the object at $t = 20$ s. Increase in the powder feed rate ($\dot{m}$) causes the maximum temperature to reduce as expected from Equation (4.44). The equation shows that the increase in $\dot{m}$ increases the power attenuation and consequently decreases the total absorbed energy. Thus, the effective energy absorbed by the substrate decreases. Further increase in the powder feed rate drops the maximum temperature below the melting temperature so that no clad can be produced. Of interest is the fact that some experiments conducted with the same process speeds but powder feed rate of $5.0e-5$ kg/s (3.0 g/min)

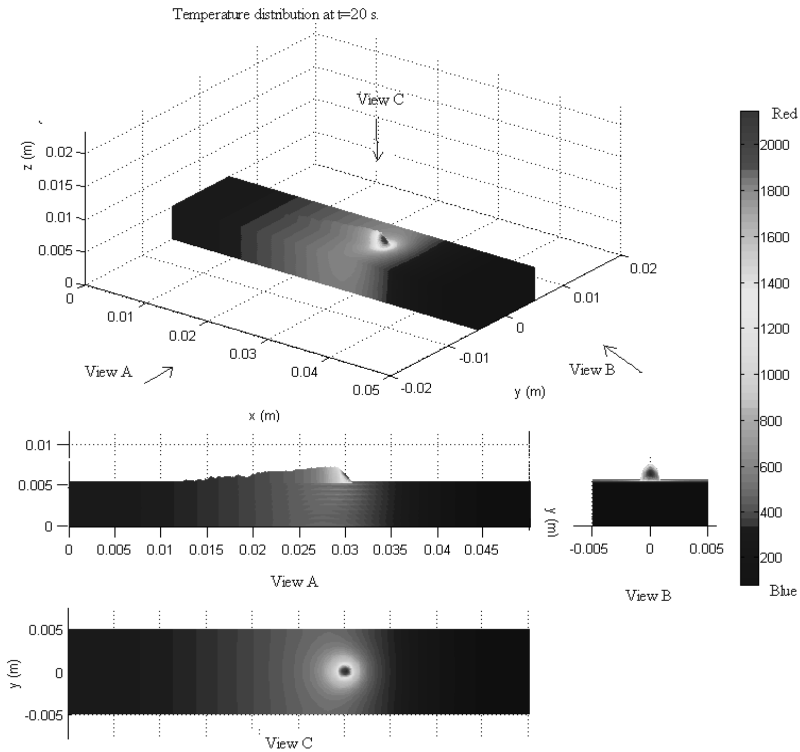

FIGURE 4.12
Temperature distribution (in Kelvin) at $t = 20$ s for a multistep laser pulse energy with $W = 0.003$ s, $F = 100$ Hz.

in which the model predicts a maximum temperature of approximately $1,800$ K showed that the cladding was impossible due to the unmelted and weak bond between the clad and substrate.

Figure 4.17 shows the melt pool at $t = 4$ and $t = 20$ s when the process velocity is 0.5 and 2 mm/s, respectively, at a powder feed rate of $1.67e - 5$ kg/s. As it is seen, the shape of the melt pool depends on the process velocity and deposited clad. The isothermal lines are also illustrated in the figure.

Figure 4.18 shows the generated clad after 20 s for a multistep velocity at $\dot{m}_1 = 1.67e - 5$ kg/s. In order to have a better view of the generated clad on the substrate, a light source to illuminate the domain is considered. As it was discussed, the ripples on the generated clad was discovered to be dependent on the size, shape and number of the elements used to mesh the domain.

Figure 4.19 shows the clad heights for different powder feed rates and different process velocities. As seen in Figure 4.19, the clad height decreases

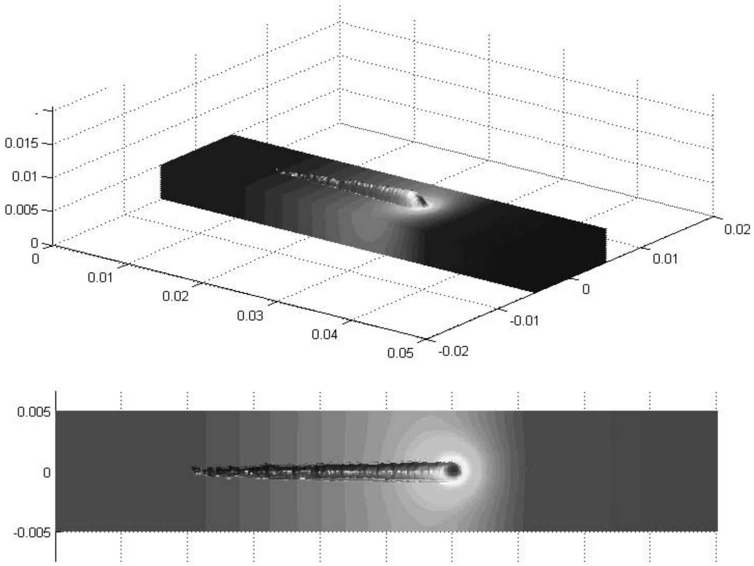

FIGURE 4.13
Generated clad after 20 s for a multistep laser pulse energy (domain is illuminated by a virtual light).

with increasing process speed, while it increases by increasing the powder feed rate as expected from Equation (4.49). The clad height is decreased gradually when the process speed is suddenly stepped up. The main reason for this occurrence is the contribution of transient temperature in the melt pool shape. The results also show that when the velocity increases, the clad height decreases. This is an indication of the nonlinearities in the process.

In order to compare the numerical and experiment results, we will next explore an experimental analysis for the evaluation of the clad quality. Then, we will use the experimental analysis along with numerical results to interpret the modeling results.

4.6.5 Experimental and Numerical Analysis

In order to validate the numerical results, an experimental analysis is performed not only to investigate the experimental dependency of laser cladding of Fe on mild steel, but also to obtain a criteria for verification of numerical results. The bases for the experimental analysis are similar to the method which will be developed in detail in Chapter 6 and is also discussed in [3, 4]. The experimental analysis relates all process parameters in Equations (2.8),

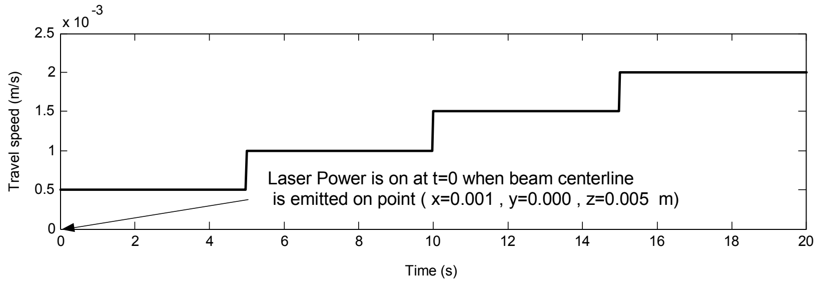

FIGURE 4.14
Multistep process speed.

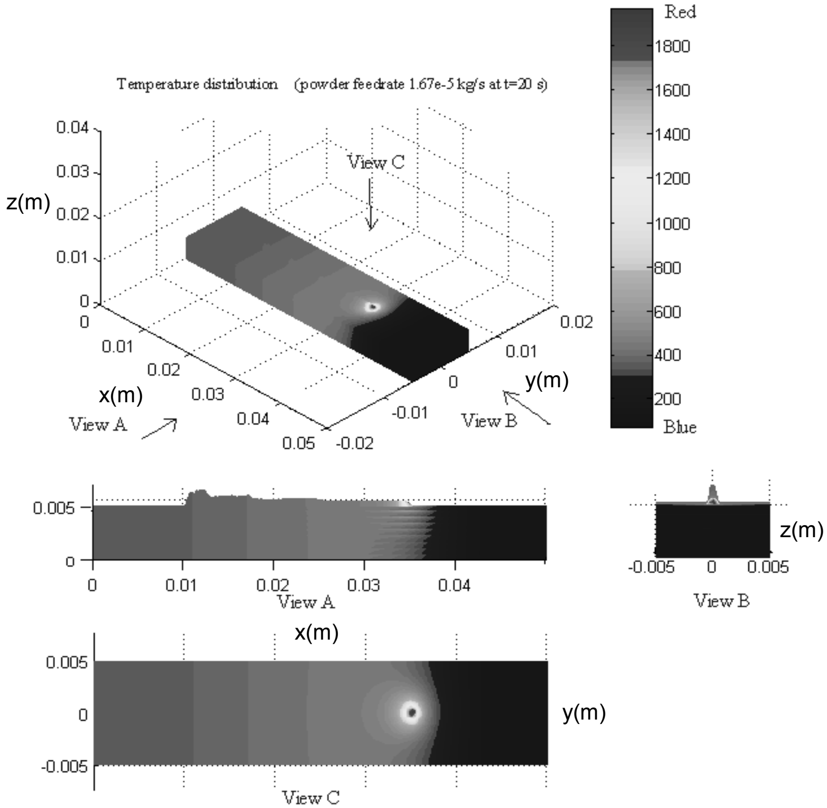

FIGURE 4.15
Temperature (in Kelvin) distribution at $t = 20$ s for a multistep travel speed ($\dot{m} = 1.67e - 5$ kg/s).

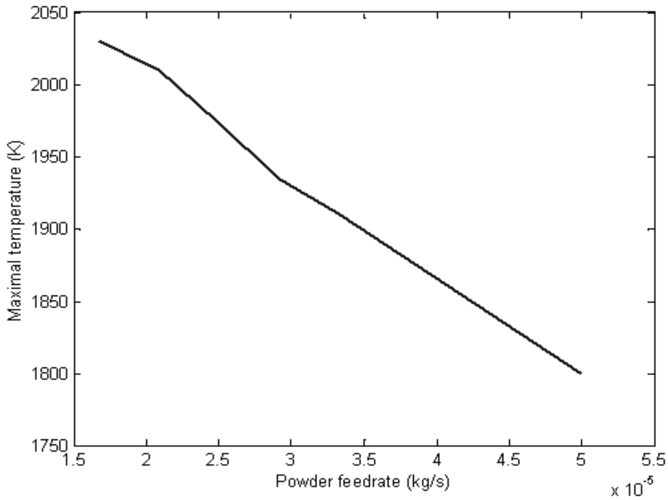

FIGURE 4.16
Maximal temperatures at $t = 20$ s for different powder feed rates ($U = 2$ mm/s).

(2.9) and (2.10), which represent the effective energy density E_{eff} [J/mm^2] and effective powder deposition density ψ_{eff} [g/mm^2] as a function of effective area A_{eff} [mm^2/s].

Calculated values for E_{eff} and ψ_{eff} of the processing conditions listed in Table 4.3 are plotted in Figure 4.20. By observation, and mechanical and metallurgical tests, four regions are distinguishable for the generated clads as shown in Figure 4.20. The region called "good quality clad" provides a good bond between the substrate and clad where the clad has a relatively smooth surface and good profile without cracks and pores. The region called "roughness, some bonding" indicates that the clad has some bonding with the substrate; however, the clad has many cracks and pores and may be easily removed from the substrate after the process. The region called "brittle" indicates that the clad has been generated without any bonds to the substrate and even the clad itself may be brittle (i.e., poorly consolidated). The region called "no cladding" indicates that no clad can be created in this region. The evidence is shown in Figures 4.21 through 4.24, which are explained in the following sections.

4.6.5.1 Experimental Setup

The experiments were performed using a 1000 W LASAG FLS 1042N Nd:YAG pulsed laser, a 9MP-CL Sulzer Metco powder feeder unit, and a 4-axis CNC table. The spot point diameter on the workpiece was set to 1.4 mm where the

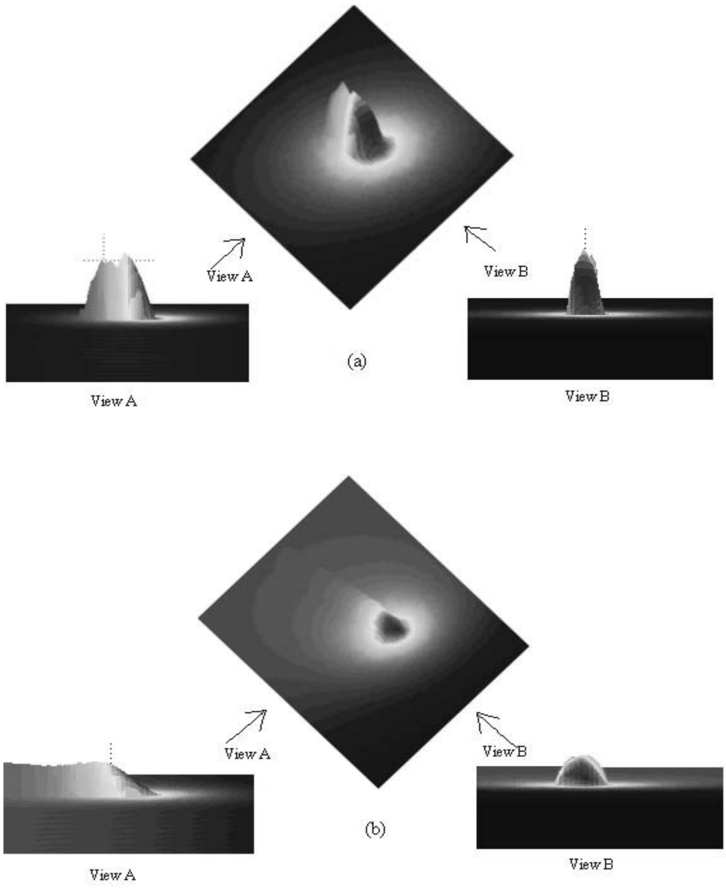

FIGURE 4.17
Temperature distribution and clad shape in different views at a) $t = 4\,\mathrm{s}$, $U = 0.5$ mm/s and $\dot{m} = 1.67e - 5$ kg/s, b) $t = 20\,\mathrm{s}$, $U = 2$ mm/s and $\dot{m} = 1.67e - 5$ kg/s.

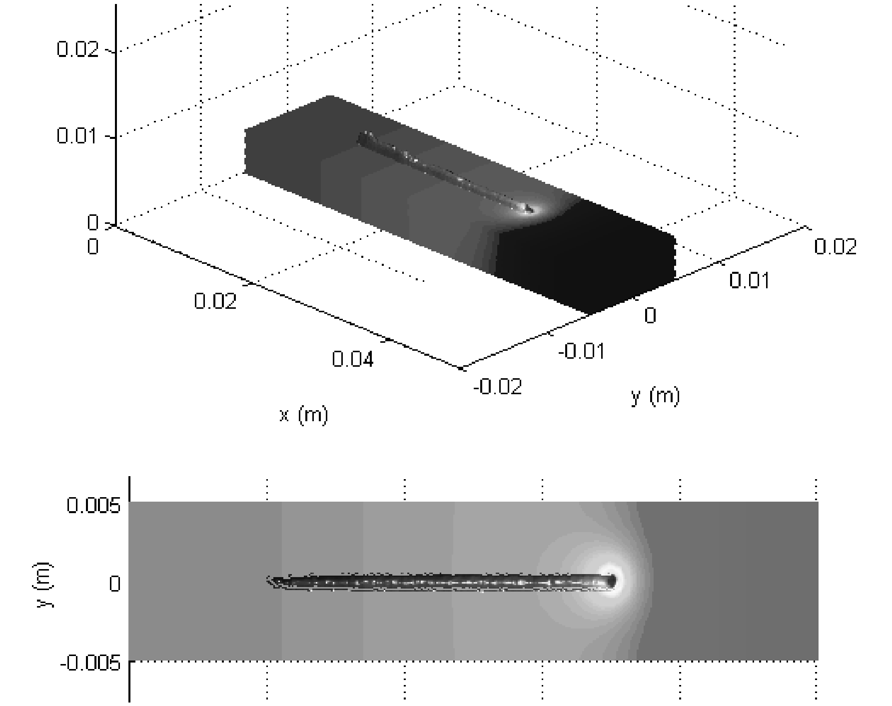

FIGURE 4.18
Generated clad at $t = 20$ s for a multistep travel speed (domain is illuminated by a virtual light).

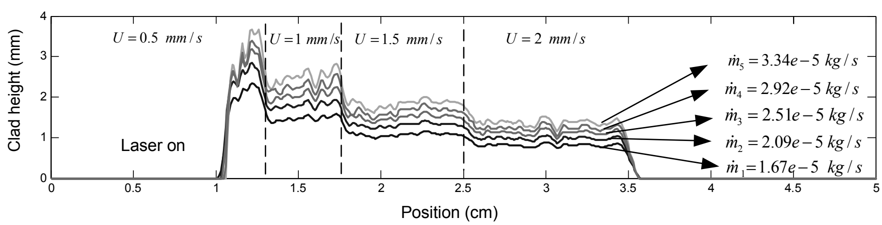

FIGURE 4.19
Numerical results for the clad heights at different powder feed rates ($\dot{m}$) and process velocities (U).

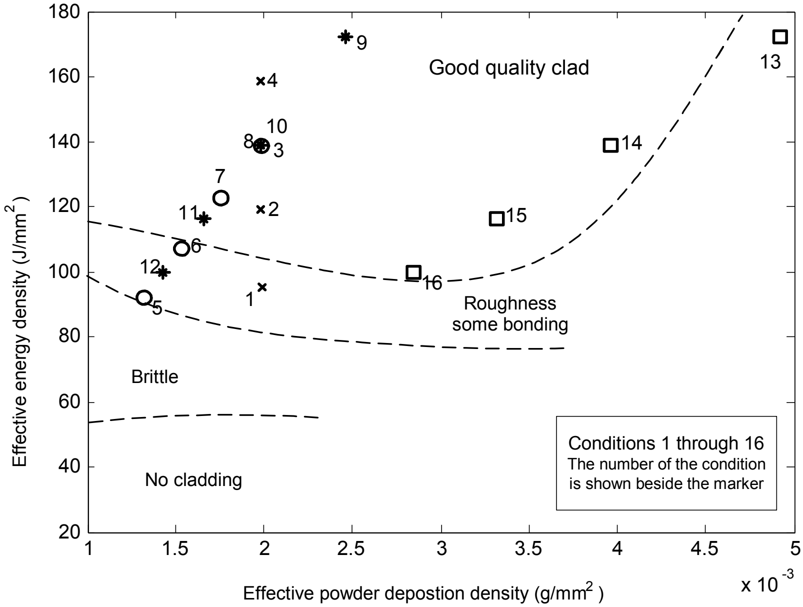

FIGURE 4.20

Effective energy versus effective powder deposition densities for conditions 1 to 16 of cladding of pure iron on the mild steel.

laser intensity was Gaussian. The laser beam was shrouded by argon shield gas. In the experiments, Argon as the shield gas and inert gas were set to $2.34e-5$ m^3/s (3 SCFH). The angle of the nozzle spray was set to 55° from the horizontal line and the size of powder stream profile was approximately 1.5 mm on the workpiece. The powder used in the experiments was Fe with a purity of 98% and mesh size of 45 μm (-325). Sandblasted mild steel plates (0.25 to 0.28 C; 0.6 to 1.2 Mn) with dimensions of $50 \times 10 \times 5$ mm were selected as the substrate. The laser was aimed at 10 mm away from the edge. The height of the clad was measured in real-time by the device discussed in [68].

Two sets of experiments were performed to mimic the numerical simulations as follows:

1. The laser pulse energy and laser pulse frequency were changed based on those which are shown in Figures 4.11a and 4.11b when the pulse width was fixed to 3 ms. The process speed was set to 1 mm/s for this set of experiments, similar to the numerical simulation. The powder feed rate was also set to 1 g/min ($1.67e-5$ kg/s) (Conditions 1 to 8).

2. The travel speed was changed as shown in Figure 4.14. This multistep speed is applied for two different feed rates: $1.67e-5$, and $3.34e-5$ kg/s.

TABLE 4.3
Conditions of experiments.

Condition	E [J]	F [Hz]	U [mm/s]	$\dot{m}$ [kg/s]
1	2.5	100	1	$1.67e-5$
2	3	100	1	$1.67e-5$
3	3.5	100	1	$1.67e-5$
4	4	100	1	$1.67e-5$
5	3.5	70	1	$1.67e-5$
6	3.5	80	1	$1.67e-5$
7	3.5	90	1	$1.67e-5$
8	3.5	100	1	$1.67e-5$
9	3.5	100	0.5	$1.67e-5$
10	3.5	100	1	$1.67e-5$
11	3.5	100	1.5	$1.67e-5$
12	3.5	100	2	$1.67e-5$
13	3.5	100	0.5	$3.34e-5$
14	3.5	100	1	$3.34e-5$
15	3.5	100	1.5	$3.34e-5$
16	3.5	100	2	$3.34e-5$

For these experiments laser pulse energy, laser pulse frequency and laser pulse width were set to 3.5 J, 100 Hz and $W = 3$ ms (Conditions 9 to 16), respectively.

4.6.6 Comparison Between Numerical and Experimental Results

Figure 4.21 shows the deviation between the numerical and experimental results for the change of laser pulse energy. As seen, the numerical modeling predicts a clad height which does not agree well with the experiment for Condition 1, while for Conditions 2, 3 and 4 there is a good agreement between the model and experimental results as listed in Table 4.4. Based on the quality analysis shown in Figure 4.20, it can be concluded that the quality of Condition 1 listed in Table 4.3 is not acceptable due to weak bonding between the clad and substrate. The reason for this is the lack of sufficient energy to melt the powder and substrate. As a result, the clad is easily removed from the substrate following the process as shown in Figure 4.21. Recalling the numerical modeling, the layer can be deposited only if a melt pool area on the substrate is expanded for any given time.

The same justification can be mentioned for the case when the laser pulse frequency is changed as seen in Figure 4.22. For this case, Condition 5 does not provide a deposit that is bonded to the substrate and Condition 6 provides a low quality clad with high roughness. For Conditions 7 and 8 the quality of clads are desired. The average errors between the experimental and numerical

TABLE 4.4
Numerical and experimental average clad height.

Condition #	Numerical average clad height (mm)	Experimental average clad height (mm)	Error (%)
1	0.25	0.76 (broken)	—
2	0.77	0.89	38
3	1.45	1.42	2
4	1.73	1.57	9
5	0	0.84 (broken)	—
6	0.38	1.20 (low quality)	—
7	1.20	1.10	8
8	1.44	1.23	14
9	2.02	2.51	24
10	1.51	2.01	33
11	1.11	0.91	18
12	0.82	0.73	10
13	2.18	3.80 (broken)	—
14	2.61	3.50	34
15	1.91	2.11	10
16	1.39	1.7	22

results for Conditions 7 and 8 are also listed in Table 4.4.

Figures 4.23 and 4.24 show the comparison between the clad heights obtained from the model and experiments for $\dot{m}_1 = 1.67e{-}5$ and $\dot{m}_5 = 3.34e{-}5$ kg/s. As seen in Figure 4.23, there is excellent agreement between the numerical and experimental results for Conditions 10, 11, 12, 15, and 16. The average error between the two results are listed in Table 4.4. In Figure 4.24, where $\dot{m}_5 = 3.34e{-}5$ kg/s, the experimental and numerical results are matched with an average error listed in Table 4.4, except for the starting point. Regardless of the relatively large errors between the numerical and experimental results in Conditions 9 and 13, the transient nature of the clad generation is correctly predicted by the model. At the starting point which represents Condition 13, the model shows a delay in the clad generation which is missing in the experimental results. After analyzing the quality of the clad, it was observed that the initial part of the clad on the substrate had very poor quality and was easily removed from the substrate as shown in Figure 4.24. This shows that the model has correctly predicted the melt pool temperature at the start and the delay was due to the time required for developing the melt pool after applying the laser onto the substrate.

To further investigate the clad/substrate geometrical profile and comparison between the numerical and experimental results, sections through the clad/substrate couples were made for selected samples. These sections were then mounted and polished to disclose their profiles.

Figures 4.25a and 4.25b show the clad/substrate macrostructure for Con-

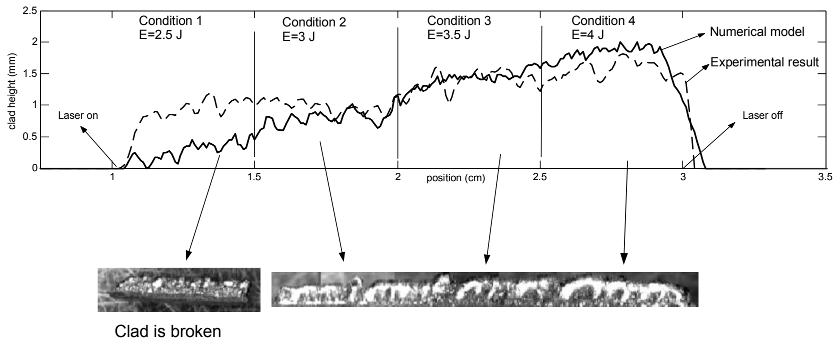

FIGURE 4.21

Comparison between the experimental and numerical results for Conditions 1 to 4.

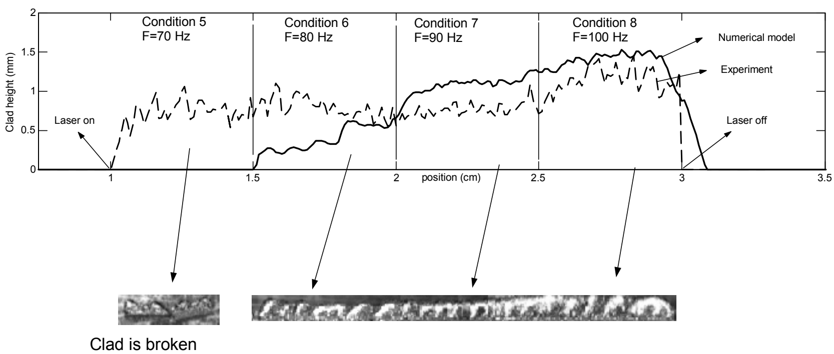

FIGURE 4.22

Comparison between the experimental and numerical results for Conditions 5 to 8.

dition 4 with a $E = 4$ J, $W = 3.0$ ms, $F = 100$ Hz and $U = 1$ mm/s and Condition 8 with a $E = 3.5$ J, $W = 3.0$ ms, $F = 100$ Hz and $U = 1$ mm/s, respectively. The clad deposit is clearly visible and the clad has a good profile. The comparison between the numerical and experimental profiles shows that the model has predicted the clad profile very well.

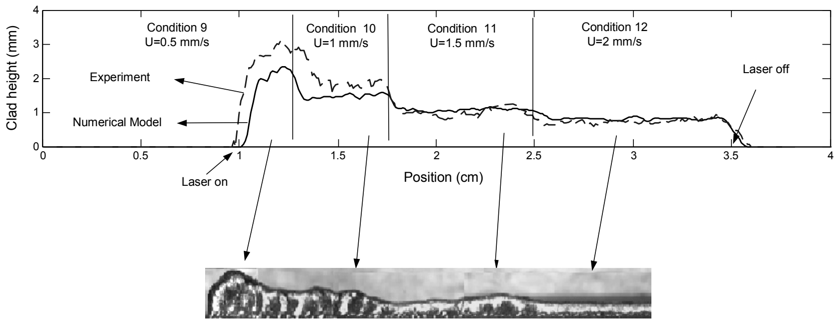

FIGURE 4.23
Comparison between experimental and theoretical data for Conditions 9 to 12 ($\dot{m}_1$= $1.67e - 5$ kg/s).

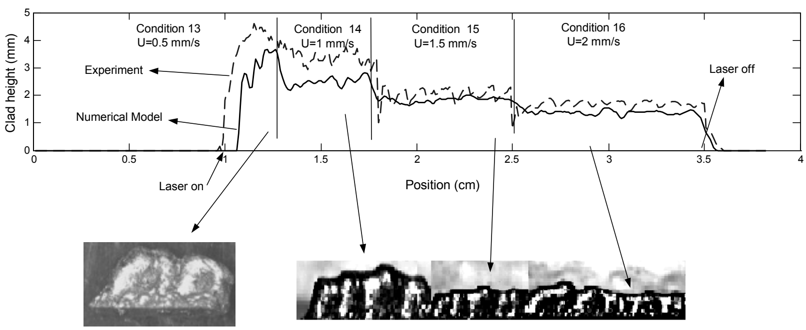

FIGURE 4.24
Comparison between experimental and theoretical data for Conditions 13 to 16 ($\dot{m}_5$= $3.34e - 5$ kg/s).

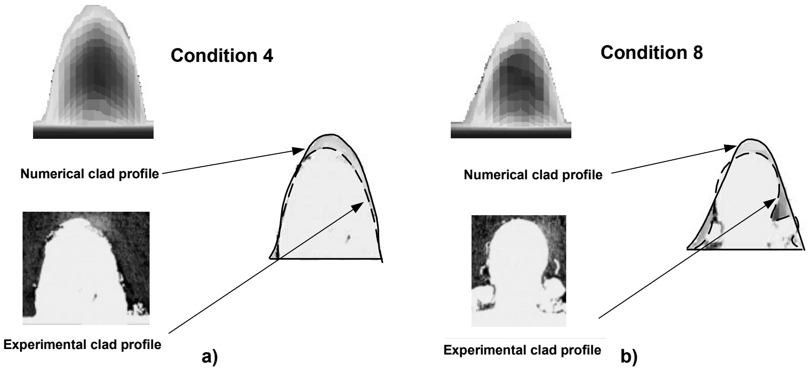

FIGURE 4.25
Comparison between numerical and experimental clads' profile for a) Condition 4, b) Condition 8.

4.7 Flow Field Modeling at the Exit of Coaxial Nozzle

This section addresses models of flow field in the exit of a coaxial nozzle. Laser cladding is a complex process involving interaction between the laser beam, the powder particles and the melted region of substrate. In order to build the clad with accurate dimensions and high efficiency of the powder deposition in a coaxial laser cladding, it is essential to analyze the powder flow structure [148]. In coaxial laser cladding, the powder is carried by a flow stream impinging on the substrate. Some designs also include a shaping gas flow helping the powder flow stream to concentrate on the melt region of the substrate. Impinging jet flow on a solid surface as used in coaxial laser cladding has applications in many industrial processes such as water jet cutting and rocket exhaust during the take off, and, therefore, it has been studied extensively [188, 189, 190]. However, for the problem of compound jets, including three different coaxial jets with the middle flow containing the powder, not much information is available. In coaxial laser cladding, three different flows are encountered. At the center, there is an air (or argon) flow for protecting the lenses from the hot powder particles that may bounce off the substrate. Next is the flow with powder particles aiming at irradiated region, and finally the shaping gas as shown in Figure 3.25. All these flows and their interactions affect the catchments of the cladding powder at the laser irradiated region, and, therefore, affect the efficiency and the quality of the clad.

Lin [191] is among the first researchers who numerically studied the powder flow structure of a coaxial nozzle for laser cladding with various arrangements of the nozzle exit. He used the commercially available FLUENT software to study the powder concentration in the air-powder flow.

The flow at the exit of the nozzle can be laminar or turbulent depending on the nozzle exit Re number. It has been shown that turbulence-free jet cannot be sustained for $Re < 1000$ [192]. Typical flow parameter values for flow at the exit of the coaxial nozzle indicate that both laminar and turbulent jet can exist depending on the size and the exit velocity of the powder stream. Therefore both flow patterns are discussed in the following.

4.7.1 Laminar Model

The governing equations for the laminar flow are Navior-Stocks and continuity equations as

$$\rho\frac{\partial \mathbf{U}}{\partial t} - \eta\nabla^2\mathbf{U} + \rho(\mathbf{U}\cdot\boldsymbol{\nabla})\mathbf{U} + \boldsymbol{\nabla}p = \mathbf{F} \tag{4.50}$$

$$\nabla\cdot\mathbf{U} = 0 \tag{4.51}$$

where $\mathbf{U}$ is velocity field [m/s], ρ is density of the gas [kg/m^3], η is dynamic viscosity [m^2/s], p is pressure field [N/m^2], $\mathbf{F}$ is external force [N].

The boundary conditions depend on the physical domain of interest. As a case study, a domain with the boundaries shown in Figure 4.26 is considered. These boundary conditions are

- On the solid surface (i.e., substrate, and solid parts of the nozzle), the conditions are set to a no-slip boundary condition, in which $v = 0$ and $u = 0$, where v and u are the velocity components [m/s].
- On the top free surface, a neutral condition is considered, in which $\mathbf{n}\cdot(\eta(\nabla\mathbf{U}) = 0$, where $\mathbf{n}$ is a normal vector on the free surfaces.
- On the side free surface, a straight out flow is considered, in which $\mathbf{t}\cdot\mathbf{U} = 0$.
- On the axisymmetric axis, the condition of slip can be considered, in which $\mathbf{n}\cdot\mathbf{U} = 0$.
- The shield gas, the powder stream, and shaping gas velocities are presented by $\mathbf{U}_l$, $\mathbf{U}_p$, and $\mathbf{U}_s$, respectively.

The physical domain can be solved by a numerical method. We developed a code using MATLAB/FEMLAB to obtain the flow field around the coaxial nozzle. The code discretized the momentum equation and generated the initial mesh in the substrate using the available options in FEMLAB. The flow domain was considered as shown in Figure 4.26. The shield gas velocity components $\mathbf{U}_l$ were set to $(0, 0.5)$, the powder stream velocity components $\mathbf{U}_p$ were set to $(0.72, 2)$, and shaping gas velocity components were set to

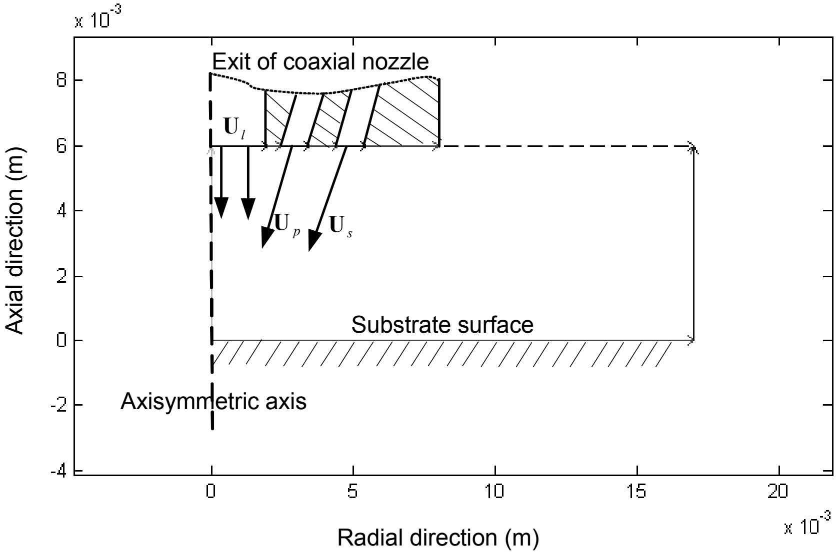

FIGURE 4.26
Geometry and boundary conditions for a typical coaxial nozzle exit ($\mathbf{U}_l$ is shield gas velocity, $\mathbf{U}_p$ is powder stream velocity, and $\mathbf{U}_s$ is shaping gas velocity).

$(0.72, 2)$. Air was selected as the carrying gas with properties of $\rho = 0.7$ kg/m^3 and $\eta = 0.000037$ m^2/s, which were the corresponding values in an average temperature of the domain under high temperature of the melt pool.

A typical flow field based on the above-mentioned boundary conditions is shown in Figure 4.27, in which the flow field is shown by arrows and surface plot of the velocity field. As seen, the dark region indicates the low or even zero velocity, whereas the brighter color illustrates the higher velocity regions. The interaction between the powder stream and shaping gas results in a complex flow pattern including the formation of a vortex close to the shaping gas as seen in the figure.

In order to investigate the trajectory of particles in the above flow field, the following equations were employed

$$m_p \frac{d(\mathbf{U}_p)}{dt} = (m_p - m_f)\mathbf{g} - 6\pi r_p \eta(\mathbf{U}_p - \mathbf{U}) \tag{4.52}$$

$$\frac{d\mathbf{x}_p}{dt} = \mathbf{U}_p \tag{4.53}$$

where m_p is particle mass [kg], m_f is fluid mass that the particle has displaced [kg], $\mathbf{U}_p$ is particle velocity vector[m/s], $\mathbf{U}$ is the fluid velocity vector [m/s],

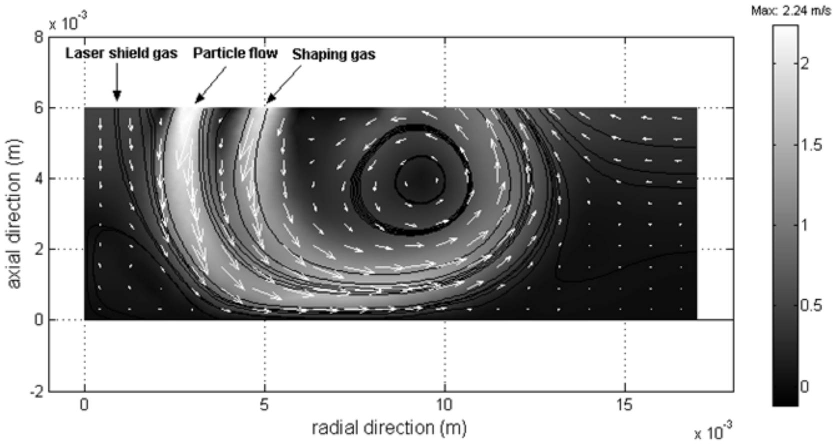

FIGURE 4.27

A typical laminar flow field at the exit of the coaxial nozzle.

r_p is particle radius [m], $\mathbf{g}$ is gravity [m/s^2], η is dynamic viscosity of the fluid [m^2/s], and $\mathbf{x}_p$ is the tracing particle position in the flow field [m]. Inherent in Equation (4.52) is the assumption that the acceleration of a particle is influenced by gravity force and drag force [193].

As a case study, Fe particles were considered with $r_p = 22.5\,\mu$m in the above velocity field. A typical trajectory of a particle is shown in Figure 4.28.

As seen, the particles follow the powder stream direction at the exit of the coaxial nozzle. However, near the melt pool, it tends to spread out due to loss of initial momentum and the existence of shield gas along the axis of symmetry.

4.7.1.1 Turbulent Flow

In this section, we investigate the flow field at the exit of the coaxial nozzle, when the flow is turbulent. In a turbulent flow, in addition to Navior-Stocks and continuity equations, the kinetic energy of turbulence k and dissipation of kinetic energy of turbulence ε should be solved. This type of turbulence modeling is referred to as $k-\varepsilon$ turbulence modeling. The general form of governing equation is presented by

$$\mathbf{U} \cdot \nabla\phi + \nabla \cdot (D_\phi \nabla\phi) = P_\phi + S_\phi \tag{4.54}$$

where

$$\phi = (u, v, k, \varepsilon) \tag{4.55}$$

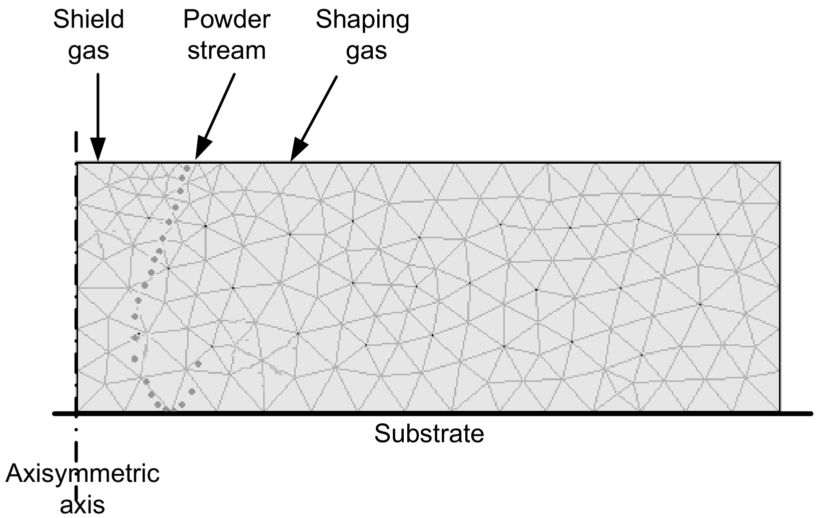

FIGURE 4.28
A typical trajectory of Fe particles in the flow field.

and D_ϕ is diffusion coefficient and S_ϕ is the source term corresponding to each ϕ components. Details of these terms can be found in the FEMLAB documentation [193].

As a case study, the above flow field was solved with the $k - \varepsilon$ turbulent model. For this model, in addition to the above laminar boundary conditions, a set of pre-defined boundary conditions in FEMLAB was used [193].

The $k - \varepsilon$ turbulent modeling capability of FEMLAB was employed to simulate the flow field. A typical result of the numerical modeling is shown in Figure 4.29.

Comparison between the laminar flow field and turbulent patterns indicates a major change in the flow field. The vortex strength is weaker and the flow streams exit the domain mainly from the side free boundary condition.

4.8 Experimental-Based Modeling Techniques

This section addresses the application of experimental-based modeling techniques including stochastic and artificial neural networks to the laser cladding process.

In many physical processes, it is very difficult or even impossible to develop an analytical model due to process complexities. In laser material processing,

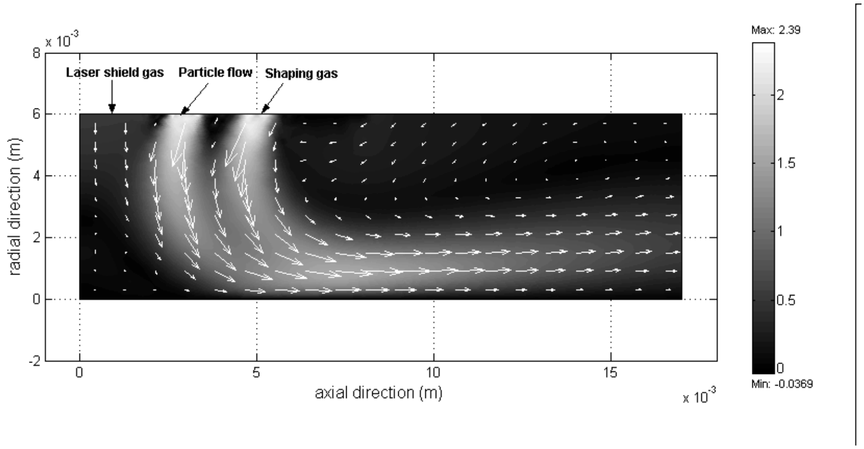

FIGURE 4.29
A typical turbulent flow field at the exit of the coaxial nozzle.

the complexity arises from the nature of the governing equations which are partial differential and also the interaction of thermal, fluid, and mass transfer phenomena in the process as addressed in Section 4.2.

There are several models for steady-state analysis of laser material processing and particularly for laser cladding [145, 160, 162, 166, 164], which provide many insights into the process. However, these models cannot be used directly in real-time control because of their limitations and intensive numerical calculations [194]. As a result, several authors have used stochastic techniques and neural network analysis to identify a dynamic model for the laser material processing. Bataille et al. [178] identified a dynamic model for laser hardening by stochastic methods. Romer et al. [171] found a dynamic model for the laser alloying process, where the table velocity or laser power was selected as the input and the melt pool surface area as the output. They used the auto regressive exogenous (ARX) system identification technique to obtain a dynamic model for the process. The authors recognized nonlinearity in the process, and, as a result, they used a linearized model around the operating point. They reported that their model performed poorly in many different cases due to its operating point dependency.

There are several papers that deal with neural network analysis for laser material processing such as laser sheet bending and laser marking. Dragos et al. [195] used an artificial neural network to predict the future shape obtained by laser bending. They used the laser power and process speed as the variable parameters and the thickness of the material as the output of the model. Peligrad et al. [196] developed a model using an artificial neural network to predict the dynamics and parameter interactions of laser marking. Their model considered the laser power and traverse speed as the inputs and the melt pool temperature as the output. However, to the knowledge of the author, there is no article on the application of neural networks for laser cladding to be used in the development of an intelligent system.

All experimental-based modeling techniques such as the stochastic, artificial neural network, and neuro-fuzzy approaches are essentially based on optimizing the parameters of a given model to result in the minimum error between the measured and model prediction data. There are basically three general model structures that are used for nonlinear model prediction, based on prior and physical knowledge [197]. These models are white-box, when the model is perfectly known; grey-box, when some physical insights are available; and black-box, when the system is completely unknown. A black-box model is much more complex compared to the other two cases due to the variety of possible model structures. One of the model structures for black box modeling is artificial neural networks. Furthermore, experimental-based modeling techniques are well developed for linear systems; however, for nonlinear systems, the techniques are very limited, and they require many considerations for the selection of the model structure, inputs/outputs, and optimization techniques used to find the system parameters.

Selecting a proper set of inputs and outputs and collecting data are critical in any dynamic model. The collected data due to the excitation signals should be rich enough and allow for identifying necessary higher modes in order to present the dynamics of the system accurately. Independent of the chosen model architecture and structure, the characteristics of the data determines a maximum accuracy that can be achieved by the model. For linear systems, a pseudo-random binary signal (PRBS) is the best choice for the excitation signal. For nonlinear systems, however, the PRBS signal is inappropriate [198]. For a nonlinear system, the minimum and maximum of amplitude and length of the excitation signals are essential to the identification process. The maximum and minimum of the amplitude reflect the range of process parameters over which the model should accurately predict the process. The magnitude of amplitude should also be changed around the desired points of operation. The length of excitation signals (duration) chosen should not be too small nor too large. If it is too small, the process will have no time to settle down, and the identified model will not be able to describe the static process behavior properly. On the other hand, if it is too long, only a very few operating points can be covered for a given signal length. The other concern about the data collection is noise within the data. The noise can arise from sensors or from the side effects of the other process parameters that are not included in the model. It is essential to generate a rich excitation signal for the data collection in terms of amplitude and duration to compensate the effects of noisy signals.

Laser cladding is a thermal process, and for a thermal process, the response to an excitation signal is essentially slow. As a result, the minimum length for excitation signals is set to 10 s. It is experimentally tested that the process response is settled down after 10 s, which indicates the required time for obtaining a steady-state response.

Laser pulse energy, width, frequency, and table velocity are important excitation signals in a laser cladding process. The clad geometry and microstructure are two geometrical and physical properties that can be selected as the output signals. In this study, different sets of inputs/outputs are selected for each experimental-based modeling technique, which will be discussed in corresponding sections.

In the following two sections, the stochastic and neural network analyses are applied to the laser cladding process and the identified models are presented.

4.8.1 Stochastic Analysis

Stochastic analysis, which is also known as system identification in engineering, is a technique to identify accurate and simplified models of complex systems from noisy time-series data. It provides tools to create mathematical models of dynamic systems based on observed input/output data. Generally, the identification procedure can be itemized as follows:

1. Design an experiment and collect input-output data from the process to be identified.

2. Examine the data and select useful portions of the original data.

3. Select and define a model structure.

4. Compute the best parameters associated with the model structure according to the input-output data and a given cost function.

5. Verify the identified model using unseen data which are not used in the identification step.

If the model verification is acceptable, the desired model is identified; otherwise, Steps 3 to 5 should be repeated by another model structure or with more data.

In order to explain the applications of stochastic analysis to laser cladding, two model structures are addressed in two separate case studies. In the first part, a model that relates the process speed to the clad height will be disclosed, and in the second part, a model that relates the laser pulse energy to the clad height will be identified.

4.8.1.1 Case Study 1: Correlation of Process Speed to Clad Height

In this section, it is intended to identify a model to relate the process speed to the clad height. The selection of these parameters as input and output is due to the focus of our research on the application of laser cladding to free forming and prototyping. A structure is selected and some knowledge about laser cladding is incorporated into the grey-box Hammerstein-Wiener model structure. In the next section, the method for data collection and experimental setup are addressed.

4.8.1.1.1 Experimental Setup and Data Collection The experiments were performed with a 350 W Lumonics JK702 Nd:YAG pulsed laser, a 9MP-CL Sulzer Metco powder feeder unit, and a CNC table. The laser power was set to 343 watts with a pulse energy of 6.86 J, width of 5 ms and frequency of 50 Hz in the experiments. The spot point was set to 5.08 mm under the focal length where the laser intensity was Gaussian. As a result, the beam diameter on the workpiece was 1.21mm. The laser beam was shrouded by Argon shield gas with a rate of $2.34e-5$ m^3/s (3 SCFH). The powder feeder has a fluidized-bed powder regulating system with a consistent feed control of the materials. In the experiments, the powder feed rate was set to 2 g/min with Argon as the shield gas at a rate of $3.93e-5$ m^3/s (5 SCFH). The angle of the nozzle spray was set to 55° from the horizontal line for experiments and the size of the powder stream was approximately 2 mm on the workpiece. The powders used in the experiments were pure Fe and Al powders, both with a purity of 98% on a metal basis and a mesh size of 45 μm (-325). These powders were mixed to a bulk composition of 20 w% Al before being placed in the powder feeder. Sandblasted mild steel plates (0.25 to 0.28 C; 0.6 to 1.2 Mn) with dimensions of $100 \times 10 \times 5$ mm were selected as the substrate.

Using this experimental setup, several experiments were performed to obtain data for the proposed model identification. Figures 4.30 and 4.31 depict two sets of data, which are obtained by two table velocities (sinusoidal and multistep) as shown in Figures 4.30a and 4.31a, respectively.

4.8.1.2 Model Prediction Using the Hammerstein-Wiener Structure

The Hammerstein-Wiener model is one of the structures used in nonlinear system identification. Several authors have studied the Hammerstein-Wiener nonlinear system for different industrial applications such as PH neutralization and distillation column [199, 200, 201].

In this case study, the Hammerstein-Wiener model structure with a more efficient algorithm is examined for the laser cladding process. Figure 4.32 shows the model structure where f and g are the Hammerstein and Wiener memoryless nonlinear elements, respectively. The addition of the nonlinear memoryless elements allows us to incorporate our physical knowledge of the process into the model while keeping the overall model as simple as possible.

In order to find the nonlinear elements of the model (f and g), we use the results reported in Romer et al. [166] and Bamberger et al. [170]. In [166, 170], the authors have shown an inverse dependency of the clad height on the square root of the relative beam velocity. They have also shown the dependency of temperature and clad height on a sigmoid function of the beam

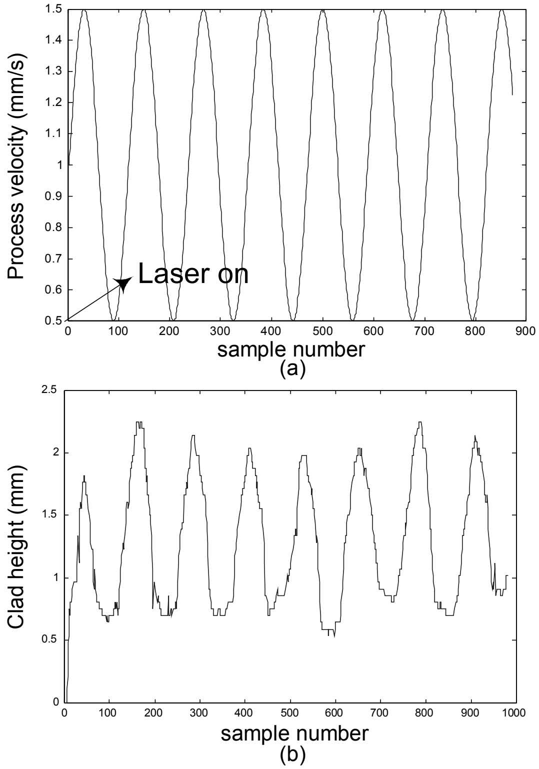

FIGURE 4.30
Experimental data, a) sinusoidal process speed, b) clad height.

velocity. As a result, it can be inferred that the clad height depends on at least two nonlinear functions in the form

$$h = f\left(\frac{1}{\sqrt{v}}, \frac{1}{1+\exp(-v)}\right) \tag{4.56}$$

This reciprocal relationship between the laser velocity and height is also evident from experimental results. Therefore, the Hammerstein-Wiener nonlinear parts of the model can be defined as:

$$f = \frac{1}{\sqrt{v}} \tag{4.57}$$

and

$$g = \frac{c_1}{c_2 + c_3 \exp(c_4 z)} \tag{4.58}$$

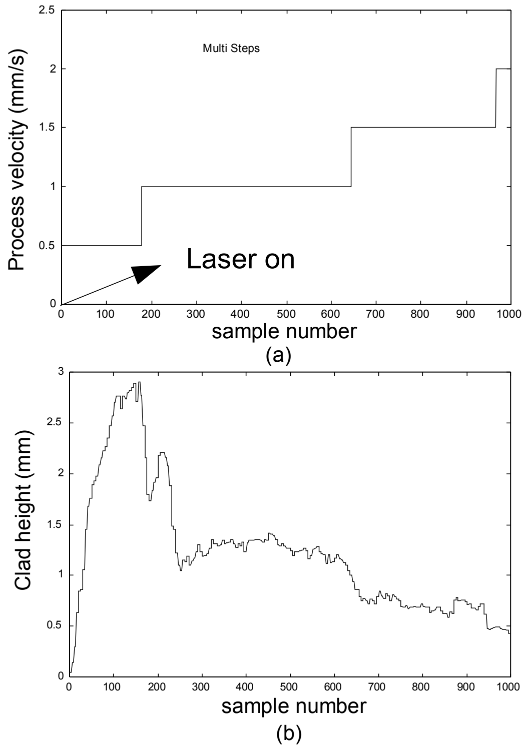

FIGURE 4.31
Experimental data, a) multi-step process speed, b) clad height.

In the Hammerstein-Wiener model structure, disturbances are modeled as additive terms in the linear part and the output signals as shown by $w(t)$ and $w^*(t)$ in Figure 4.32, respectively [200, 199].

Based on these assumptions and the notation of Figure 4.32, the output of the linear block is

$$z(t) = G(q, \theta)u^* + H(q, \theta)e(t) \tag{4.59}$$

where $G(q, \theta)$ and $H(q, \theta)$ are the linear models (rational functions) of the shift operator q for the system and disturbances, respectively, and $e(t)$ is assumed to be white noise. The other parameters are shown in Figure 4.32.

Removing the bias problem from Equation (4.59) (see [202] for details), it can be written as

$$A(q)z(t) = B(q)u^*(t) + e(t) \tag{4.60}$$

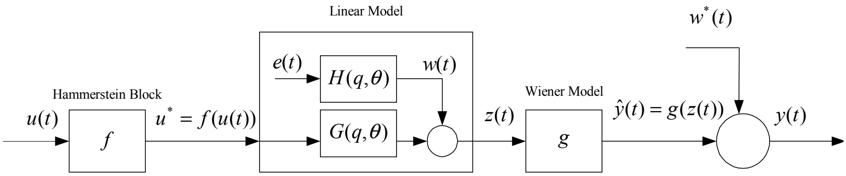

FIGURE 4.32
Hammerstein-Wiener nonlinear structure.

where

$$A(q) = 1 + \sum_{i=1}^{n_f} a_i q^{-i} \tag{4.61}$$

and

$$B(q) = 1 + \sum_{i=1}^{-(n_k+n_b-1)} b_i q^{-i} \tag{4.62}$$

and n_k, n_f and n_b are orders of the delay, denominator and numerator, respectively. Using Equation (4.60) and applying the operator q, $z(t)$, Equation (4.59) can be written as

$$z(t) = -\sum_{i=1}^{n_f} a_i z(t-i) + \sum_{i=1}^{-(n_k+n_b-1)} b_i u^*(t-i) + e(t) \tag{4.63}$$

Assuming the Wiener nonlinear part in Figure 4.32 is invertible, then

$$z(t) = g^{-1}(\widehat{y}(t)) \tag{4.64}$$

Substituting Equation (4.64) into Equation (4.63) results in

$$z(t) = -\sum_{i=1}^{n_f} a_i g^{-1}(\widehat{y}(t-i)) + \sum_{i=1}^{-(n_k+n_b-1)} b_i u^*(t-i) + e(t) \tag{4.65}$$

and $y(t)$ becomes

$$y(t) = g(z(t)) + w^*(t) \tag{4.66}$$

In general, all linear and nonlinear parameters are included in the optimization procedure to minimize the output error [202]. However, implementation of this algorithm usually suffers from numerical divergence. In the following, an improved algorithm is proposed to predict the model parameters. Since the Hammerstein part of the system is assumed to be known for the laser cladding process, the algorithm only identifies the linear and Wiener nonlinear parts. The steps of the algorithm are:

1. Remove the mean value from the output data $y(t)$.

2. Ignore the Wiener block g; guess the order of linear part $\widehat{G}$.
3. Use $u^*(t)$ and $y(t)$ as the input and output; find the primary linear model $\widehat{G}$.
4. Repeat steps 2 and 3 by changing the order of the linear model to minimize $\sum(y(t) - z(t))^2$ where $z(t)$ is the output of the linear system.
5. Find the nonlinear parameters of $g(z)$ based on $z(t)$ using Gauss-Newton minimization method.
6. Find $z^*(t) = g^{-1}(y(t))$.
7. Re-identify the linear model based on $u^*(t)$ and $z^*(t)$.
8. Repeat from Step 5 until $|\varepsilon_1^k + \varepsilon_2^k - (\varepsilon_1^{k-1} + \varepsilon_2^{k-1})| \leq \delta$ where k and δ are the iteration index and a small positive number, respectively, and: $\varepsilon_1^k = \|\theta_k\|$, $\varepsilon_2^k = \|y_k(t)\|$.

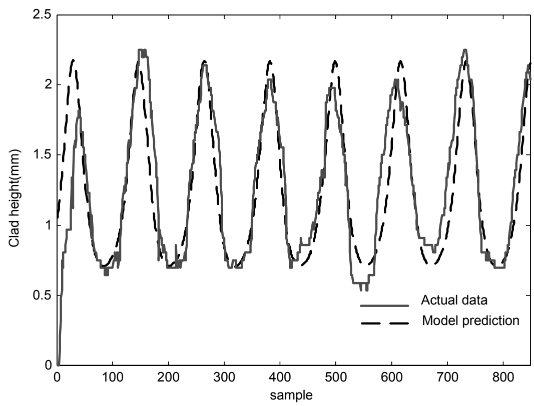

FIGURE 4.33
Comparison of actual data and Hammerstein-Wiener model prediction.

Code was written in MATLAB using the System Identification Toolbox to implement the above algorithm for the structure shown in Figure 4.32. This code was applied to the collected data of the laser cladding process.

During the parameter estimation, it was observed that there was an optimum order for the linear subsystem such that increasing or decreasing the order resulted in higher prediction error. The overall structure of the system was relatively simple; however, the optimization algorithm was very sensitive

TABLE 4.5
Hammerstein-Wiener model parameters.

a_1	-1.0764	a_6	0.0235	b_4	-0.0196
a_2	-0.0672	a_7	0.0924	c_1	0.1570
a_3	0.0610	b_1	0.0035	c_2	0.0020
a_4	-0.0069	b_2	0.0700	c_3	1.0125
a_5	0.0024	b_3	-0.0265	c_4	-1.6722

to the order of linear part as well as to initial parameters of the nonlinear block. The optimum value for the order of the linear subsystem was 7 for the denominator and 4 for the numerator with a delay of 1. A sample time of 0.08 s was used in the identification process. Table 4.5 lists the estimated parameters according to Equations (4.58) and (4.65).

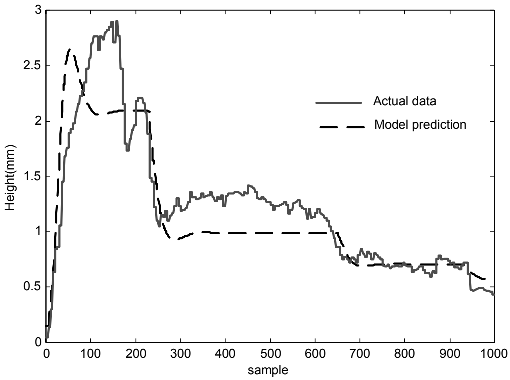

FIGURE 4.34
Verification of Hammerstein-Wiener model.

Figure 4.33 compares the experimental data with the model predictions when the sinusoidal data shown in Figure 4.30 are used. As seen in Figure 4.33, good agreement between the model and experimental results is achieved. Because of the effects of other involved parameters such as instability of powder feeder spray, dependency of the beam reflectivity and focal point to the clad height, there are some discrepancies between the predicted and actual data.

To verify the identified model, the multistep response shown in Figure 4.31a was applied to the estimated model. The simulation and actual data are compared in Figure 4.34. To evaluate the effect of the Wiener nonlinear block on the overall system output, the results of the model without the Wiener structure are compared with the experimental data as shown in Figure 4.35. As seen in the figure, the nonlinear Wiener block has significantly improved the identified model.

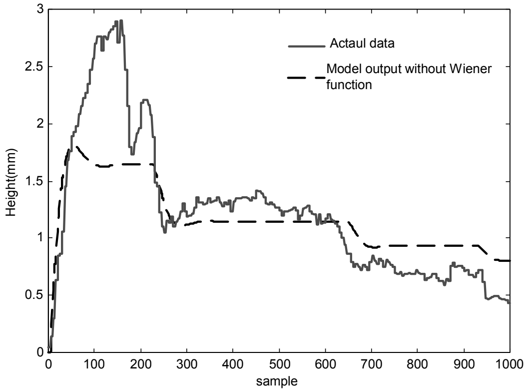

FIGURE 4.35
Effect of elimination of Wiener function on model prediction.

The identified model using the Hammerstein-Wiener model structure offers a simple and relatively accurate model for the laser cladding process. The sluggish nature as well as large settling time associated with laser cladding can be predicted very well by the model. This model will be used for designing a controller in Chapter 5.

4.8.1.3 Case Study 2: Correlation of Laser Pulse Energy to Clad Height

In the second part of the stochastic analysis, it is intended to identify a model to relate the laser pulse energy to the clad height. Experimental analysis shows that the energy has a linear relationship with the clad height about a desired operating point. Since there are many non-linear uncertainties in the process, it is essential to select an operating point and consider only small variations of the input signal around this operating point. The choice of operating point is determined by the quality of clad as a constraint in the process identification. This issue will be addressed in Chapter 6.

Providing the above-mentioned requirements, the identification of a model that reflects the dynamics of the process due to the changes in the laser pulse energy can be carried out using a classic ARX method [202], which will be discussed later. In the following section, the experimental setup and the selected data for the identification process will be addressed.

4.8.1.3.1 Experimental Setup and Data Collection The experiments were performed with a LASAG FLS 1042N Nd:YAG pulsed laser with a maximum of 1000 W power, a 9MP-CL Sulzer Metco powder feeder unit, and a 4 axis CNC table. The spot point on the workpiece was 5.08 mm under the focal point with a diameter of 1.4 mm where the laser intensity was Gaussian. The laser beam was shrouded by Argon shield gas with a rate of $2.34e - 5$ m^3/s (3 SCFH). In the experiments, the powder feed rate was set to 1 g/min with Argon as the shield gas at a rate of $2.34e - 5$ m^3/s (3 SCFH). The angle of the nozzle spray was set to 55° from the horizontal line for experiments and the size of powder stream profile was approximately 1.4 mm on the workpiece. The powders used in the experiments were pure Fe and Al powders both with a purity of 98% on a metal basis and a mesh size of 45 μm (-325). These powders were mixed to a bulk composition of 20 w% Al before being placed in the powder feeder. Sandblasted mild steel plates (0.25 to 0.28 C; 0.6 to 1.2 Mn) with dimensions of $100 \times 10 \times 5$ mm were selected as the substrate. The clad height was measured by the device discussed in Chapter 3.

Several sets of PRBS pulse energy signals around 3.5 J were applied to the apparatus as shown in Figures 4.36 and 4.37 when U = 1.5 mm/s, $\dot{m}$ = 1 g/min, F = 96 Hz and W = 3 ms.

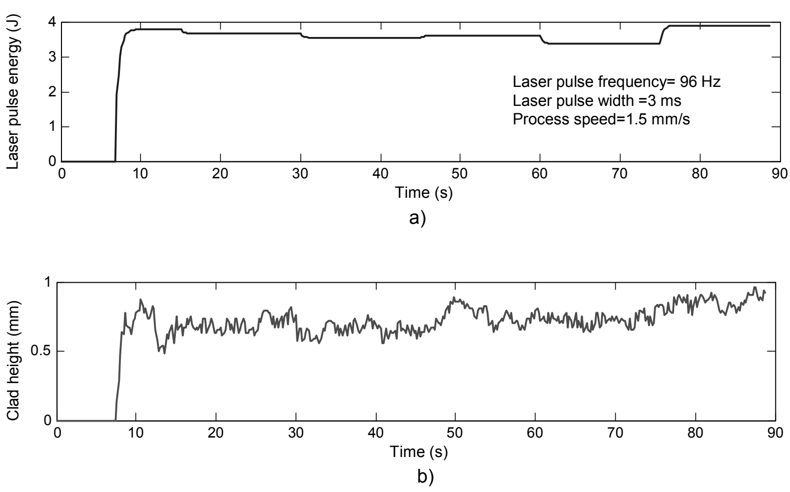

FIGURE 4.36
Experimental data, a) random laser pulse energy, b) clad height.

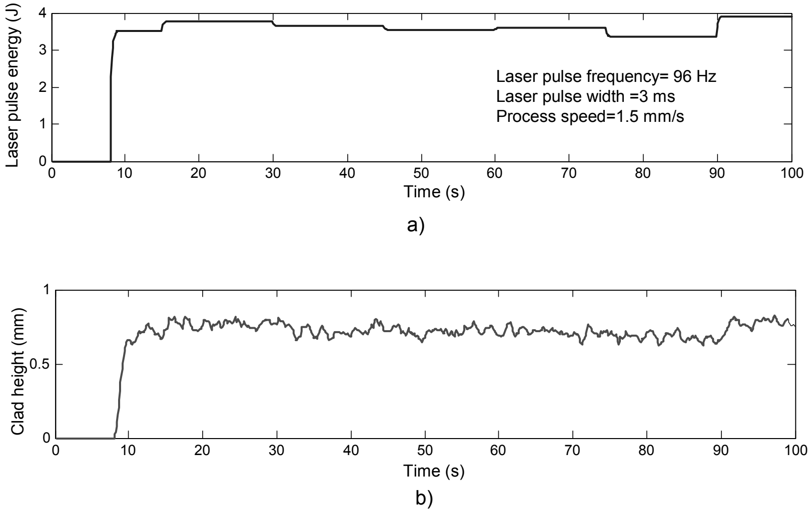

FIGURE 4.37
Experimental results for random excitation signal, a) laser pulse energy, b) clad height.

4.8.1.3.2 ARX Model The auto regressive exogenous (ARX) system identification is one of the structures used in linear system identification. It is the most popular model structure, which describes the error by means of white noise [202]. A simple input-output model that can be considered for a linear, time-variant, discrete-time and single-input single-output (SISO) system (see Figure 4.38) is

$$D(q)y(t) = C(q)u(t) + e(t) \tag{4.67}$$

where $y(t)$ and $u(t)$ are output parameter and input, respectively, $e(t)$ is the white noise, $D(q)$ and $C(q)$ are functions of shift operator q in the discrete space and are denominator and numerator, respectively. These functions can be presented by

$$C(q) = c_1 q^{-1} + ...c_{n_b} q^{-n_c} \tag{4.68}$$

$$D(q) = 1 + d_1 q^{-1} + ...d_{n_a} q^{-n_d} \tag{4.69}$$

where c_i and d_i are the coefficients of the polynomials, n_c and n_d are the order of $C(q)$ and $D(q)$, respectively.

Code was developed in MATLAB using its System Identification Toolbox to implement the ARX model structure shown in Figure 4.38. This code was applied to the collected data of the laser cladding process. During the parameter estimation, it was observed that an optimum order for the linear

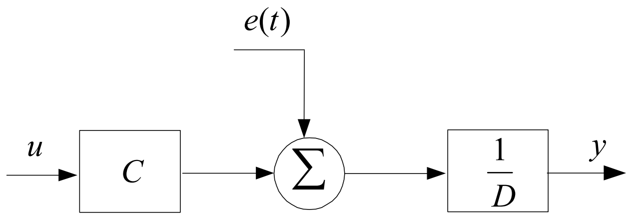

FIGURE 4.38
ARX model structure.

TABLE 4.6
ARX model parameters.

d_1	-0.5807
d_2	-0.2305
c_1	0.03834

system was 2 for the denominator $D(q)$ and 1 for the numerator $C(q)$. Table 4.6 lists the estimated parameters according to Equations (4.68) and (4.69). Several different orders were checked to investigate their effects on the model. However, results showed that increasing the order of the linear model does not reduce the overall error. As a result, the above-mentioned orders were selected for the model identification.

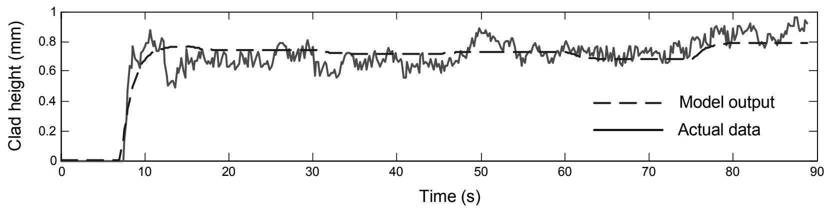

FIGURE 4.39
Comparison between the experimental and modeling results.

Figure 4.39 compares the experimental data with the model predictions when the PRBS shown in Figure 4.36a was used. As seen in Figure 4.39, good agreement between the model and experimental results is achieved.

To verify the identified model, a set of unused data in the identification procedure, which was generated by a different PRBS shown in Figure 4.37a, was fed to the identified model. The simulation and actual data are compared

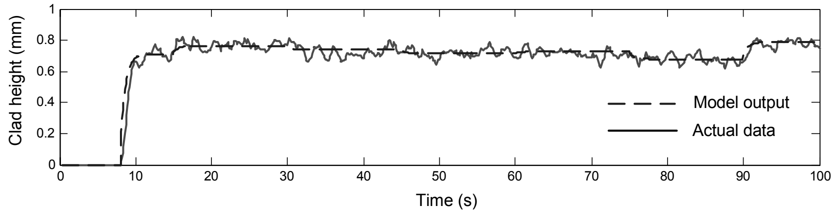

FIGURE 4.40
Verification of the ARX model structure.

in Figure 4.40. As shown, good agreement has been achieved.

Several different models with the same orders and delay are identified around different operating points using the same strategy. These models are then used for controller design and also as a base for tuning the controller gains in the virtual atmosphere as will be discussed in Chapter 5.

4.8.2 Artificial Neural Network Modeling

Artificial neural networks have gained prominence recently among researchers of manufacturing technologies. As the name implies, these networks are computer models of the process that constitute biological nervous systems. In recent years, there have been continuous publication of studies focusing on the improvement of the artificial neural network techniques. Many researchers have applied the artificial neural network to different processes to obtain their precise models. However, to the best knowledge of the author, there is no article on the application of neural networks to laser cladding to be used in development of an expert system.

The most important characteristics of neural networks are: made from a large number of perceptron units, strongly connected units, robustness against the failure of single units, and learning from data. Although neural networks can be trained to solve problems that are difficult for conventional computers or humans, selecting an appropriate model structure for a particular problem is still a big challenge. This challenge is more noticeable in dynamic systems where memory elements are required for accurate system modeling.

Neural networks as shown in Figure 4.41 are basically composed of simple elements called perceptrons. Each perceptron has multiple inputs with processing elements including a summation and an activation unit. The network's function is determined largely by the connections between the processing elements. The signals flowing between the perceptrons are scaled by adjustable parameters called weights.

A neural network can be trained to perform a particular function by adjusting the weights. Usually, neural networks are adjusted or trained so that a particular set of inputs leads to a specific set of target outputs. Typically,

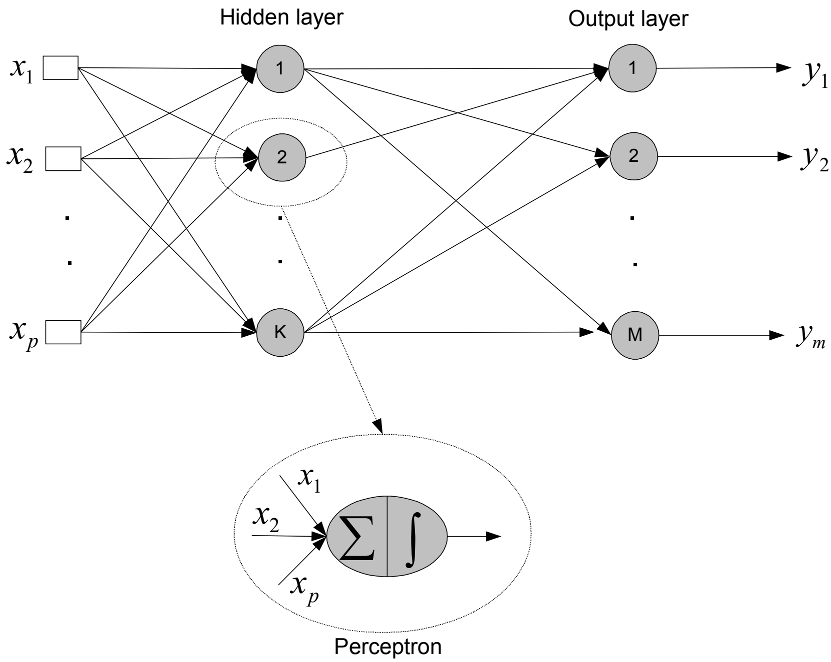

FIGURE 4.41
A multilayer perceptron with one hidden layer.

many input/output pairs are used to train a network. One of the methods used to train a neural network is backpropagation given by Principe et al. [203].

4.8.2.1 Neural Network Analysis for Laser Cladding – Case Study

In this study, a recurrent neural network structure is applied to laser cladding by powder injection to predict the clad height and rate of solidification. The prediction, simulation, optimization, and verification are performed for the process identification. For identification, the process velocity and laser pulse shaping including laser pulse energy, laser pulse frequency and laser pulse width as the inputs, and the clad height and rate of solidification as the outputs are used, which are shown in Figure 4.42. Of interest is the fact that the rate of solidification has a direct relationship with clad microstructure [204] and can be considered a measure for microstructure evaluation.

In the next section, the experimental setup and data collection will be addressed.

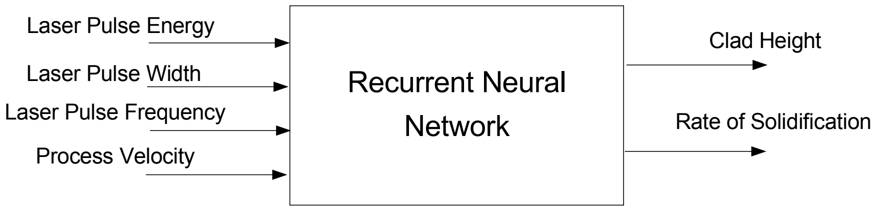

FIGURE 4.42
Inputs and outputs to the recurrent neural network.

4.8.2.1.1 Experimental Setup and Data Collection The experiments were performed with the same experimental setup discussed in Section 4.8.1.3.1. However, in order to develop a comprehensive model to reflect the influence of essential process parameters, in addition to those experiments shown in Figures 4.36 and 4.37, numerous other experiments were performed to create a robust model. A large set of data with different specifications was obtained in different working conditions. For instance, the laser pulse energy was increased in several steps as shown in Figure 4.43a, while the other process parameters were held constant as shown in the figures. Figures 4.43b, and 4.43c also show the output results, which are clad height and rate of solidification versus time for any of the multistep laser pulse energy excitation signals.

In the next section, the selected structure for the model identification using the artificial neural network will be discussed, and the results of identification will be presented.

4.8.2.1.2 Elman Recurrent Neural Network Model Architecture A recurrent neural network as shown in Figure 4.44 is a particular form of neural network model that has a feedback signal in the network architecture. This feedback enables the network to be used in problems and applications that require state representation such as speech processing, plant control, adaptive signal processing, time series prediction, and so on. The universal approximation capabilities of the recurrent multilayer perceptron make it a popular choice for modeling nonlinear dynamic systems and implementing general-purpose nonlinear controllers [205].

There are different forms of recurrent neural networks such as Elman and Hopfield networks. The Elman network is a two-layer network with feedback from the first output layer to the first input layer [206] as shown in Figure 4.44. In the figure, **u** and **y** are the input and output matrices, respectively, **IW** are the network's weights, **LW** is the feedback weight, **D** is the delay and **b** is the bias matrix. This recurrent connection allows the Elman network to both detect and generate time-varying patterns for approximating any dynamic systems with an arbitrary accuracy. The only requirement is that the hidden

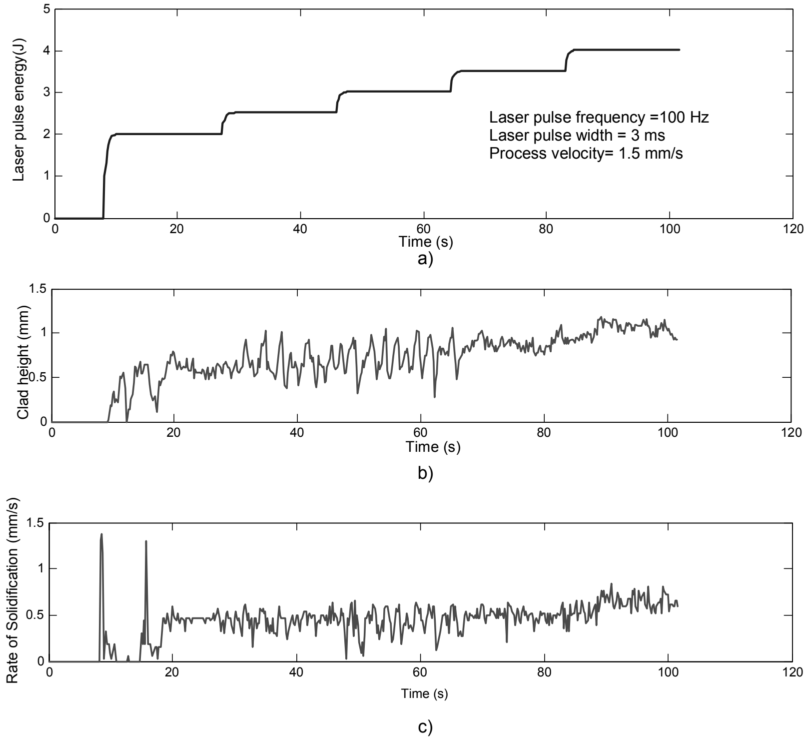

FIGURE 4.43

Step excitation signal showing: a) laser energy vs. time, b) clad height vs. time, c) rate of solidification vs. time.

layer must have a suitable number of neurons. Although more hidden neurons are needed as the complexity of the function's being fit increases, increasing the number of hidden neurons causes noise identification instead of process identification in a noisy environment [207].

For the laser cladding process model prediction, an Elman recurrent neural network as shown in Figure 4.44 was implemented. The delay **D** was selected as 2 samples due to the observed delay between the excitation signal and the real process response. The number of neurons were 12 and 2 for hidden and output layers, respectively. The significance of the number of neurons has a direct relationship with training performance for noisy data. Selecting less than 12 neurons causes the network to be inaccurate in prediction, while higher number of neurons causes the network to model noise instead of the process dynamics. When more neurons are used, the training method tries to fit the model into the noisy data by adjusting the weights and biases, and, as a result, the identified model cannot predict the process very well.

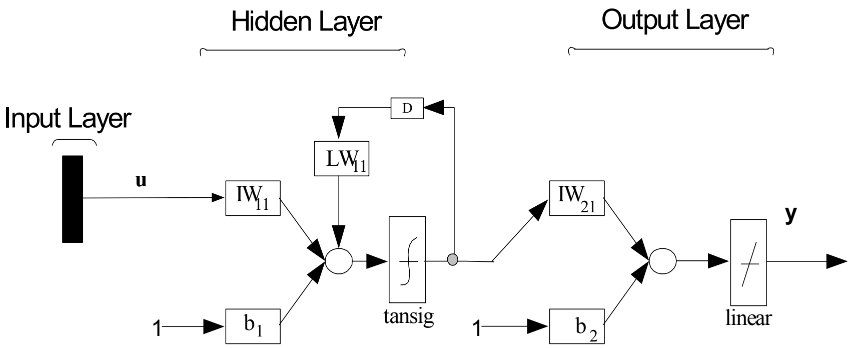

FIGURE 4.44
Elman recurrent neural network.

To train the network, backpropagation through the time technique [203] with 4, 309 sets of input/output data were used. Figure 4.45 shows the training performance. As seen, the network converged to 0.0422 after 14 epochs, which is the sequence of training. However, due to the noise within the data, a better performance cannot be achieved. It seems that there is a minimum point in the selected data which causes the training to be stuck at that local minimum. The training results in the weight matrices are listed in Table 4.7.

After training, the network was simulated. The same inputs as shown in Figures 4.43a and 4.36a were initially fed into the trained network. The simulation results for the clad heights are shown in Figures 4.46 and 4.47. Also, Figure 4.48 illustrates the comparison between the rate of solidification obtained from the model and process. As seen, the trained network is able to predict the outputs relatively well.

In order to validate the identified model, several sets of unseen and new data in the training procedure were fed into the network. As seen in Figure 4.49a, a multistep laser pulse frequency is fed into the network when the laser pulse energy, laser pulse width and process velocity are fixed. Figures 4.49b and 4.49c show comparison of the model output with the actual data. The figures indicate good agreement between the model and actual data. Verification confirms that the model has a good potential to predict the transient behavior of the process due to the suitable neural network structure and a large variety within the data fed into the model.

TABLE 4.7
The RNN matrices of layers.

LW_{11}											
0.578	0.1731	-0.247	-0.757	0.513	0.550	0.332	-0.575	-0.200	0.152	-0.002	-0.753
0.403	-0.642	-0.147	0.246	-0.500	0.389	-0.407	0.659	-0.638	0.672	-0.313	0.478
-0.122	-0.406	-0.420	0.490	-0.231	0.983	-0.110	0.441	-0.656	-0.461	0.377	0.264
0.200	0.180	-0.147	-0.361	0.034	0.096	-0.542	0.575	-0.746	0.644	0.758	0.099
0.670	-0.482	-0.318	-0.353	0.323	-0.721	0.695	-0.431	0.0990	-0.591	0.395	-0.379
0.305	0.263	-0.231	0.454	0.151	0.210	-0.314	-0.097	-0.824	-0.948	0.362	0.702
-0.415	-0.418	0.005	0.467	-0.064	0.520	-0.740	-0.688	0.0363	-0.437	-0.606	-0.389
-0.210	0.125	0.317	0.694	-0.078	0.681	0.364	0.5016	-0.547	0.619	-0.578	0.363
-0.487	0.010	-0.302	-0.041	-0.642	-0.433	0.616	0.097	0.420	-0.681	-0.756	0.248
-0.020	-0.074	-0.823	0.855	-0.120	0.432	-0.454	-0.383	-0.265	-0.500	-0.449	-0.607
-0.173	0.080	-0.109	-0.093	-0.255	0.042	-0.476	-0.240	0.619	0.956	0.606	0.195
-0.050	0.612	-0.046	0.421	-0.273	0.599	0.599	0.509	-0.627	-0.399	0.671	0.145
IW_{11}						b_1				b_2	
0.233	-0.002	-0.004	-0.146			-2.18				-0.609	
0.070	-0.003	-0.006	-0.190			-1.553				-0.628	
0.168	-0.009	-0.018	0.592			-1.521					
-0.521	-0.003	-0.005	-0.178			1.443					
-0.144	.0031	0.062	0.210			0.575					
-0.079	0.006	0.012	0.390			0.430					
0.737	-0.003	-0.007	-0.241			0.392					
0.166	-0.003	-0.006	-0.191			-0.016					
0.146	0.003	0.005	0.166			0.244					
-0.046	-0.016	-0.021	-0.704			-0.982					
0.512	0.007	0.014	0.469			0.518					
-0.247	0.003	0.005	0.185			-1.204					
IW_{21}											
0.079	0.032	0.791	0.200	0.982	-0.153	-1.077	0.1501	-0.634	-0.780	0.133	0.357
-0.616	-0.643	0.320	0.410	-0.999	0.523	-0.653	-0.793	-0.965	0.046	0.433	-0.029

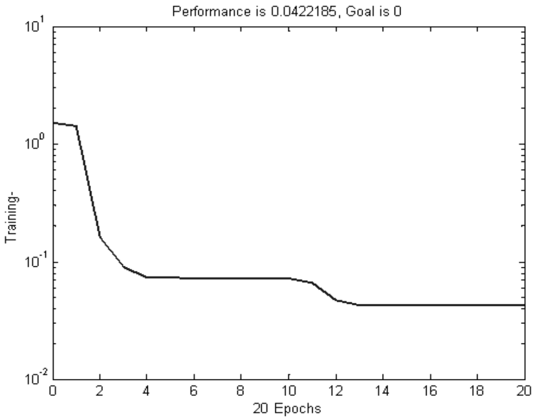

FIGURE 4.45
Training performance.

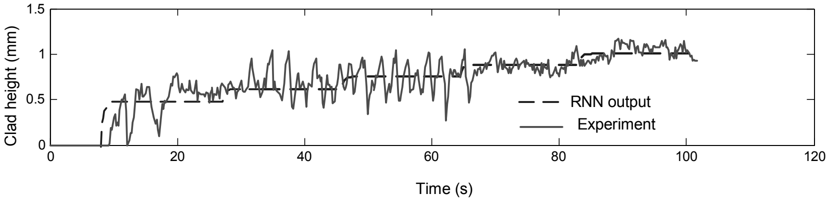

FIGURE 4.46
Comparison between model and experiments for the clad height for the multistep laser pulse energy excitation.

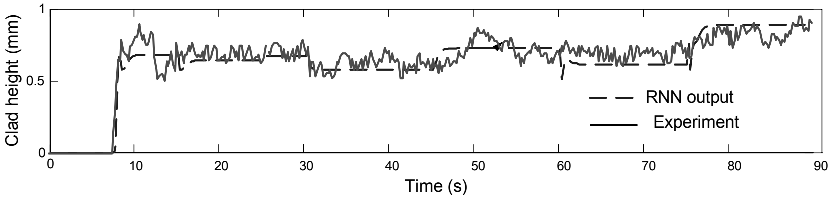

FIGURE 4.47
Comparison between model and experiments for the clad height for random laser pulse energy excitation.

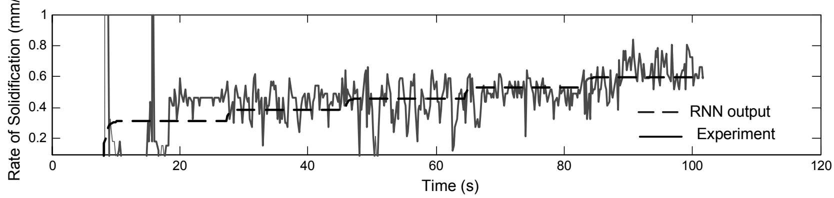

FIGURE 4.48
Comparison between model and experiments for the rate of solidification for the multistep laser pulse energy excitation

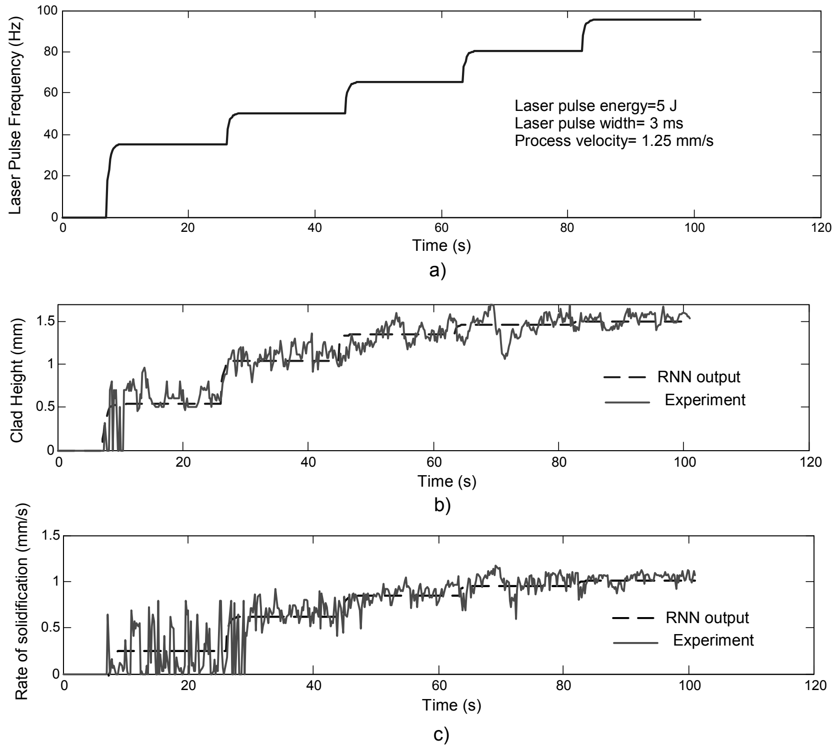

FIGURE 4.49
Data for verification: a) Multistep laser pulse frequency, b) Verification of model for the clad height for multistep laser pulse frequency, c) Verification of model for the rate of solidification for multistep laser pulse frequency.